iScience

CellPress
OPEN ACCESS

Article

Nitrogen-doped nanoporous graphene induced by a multiple confinement strategy for membrane separation of rare earth

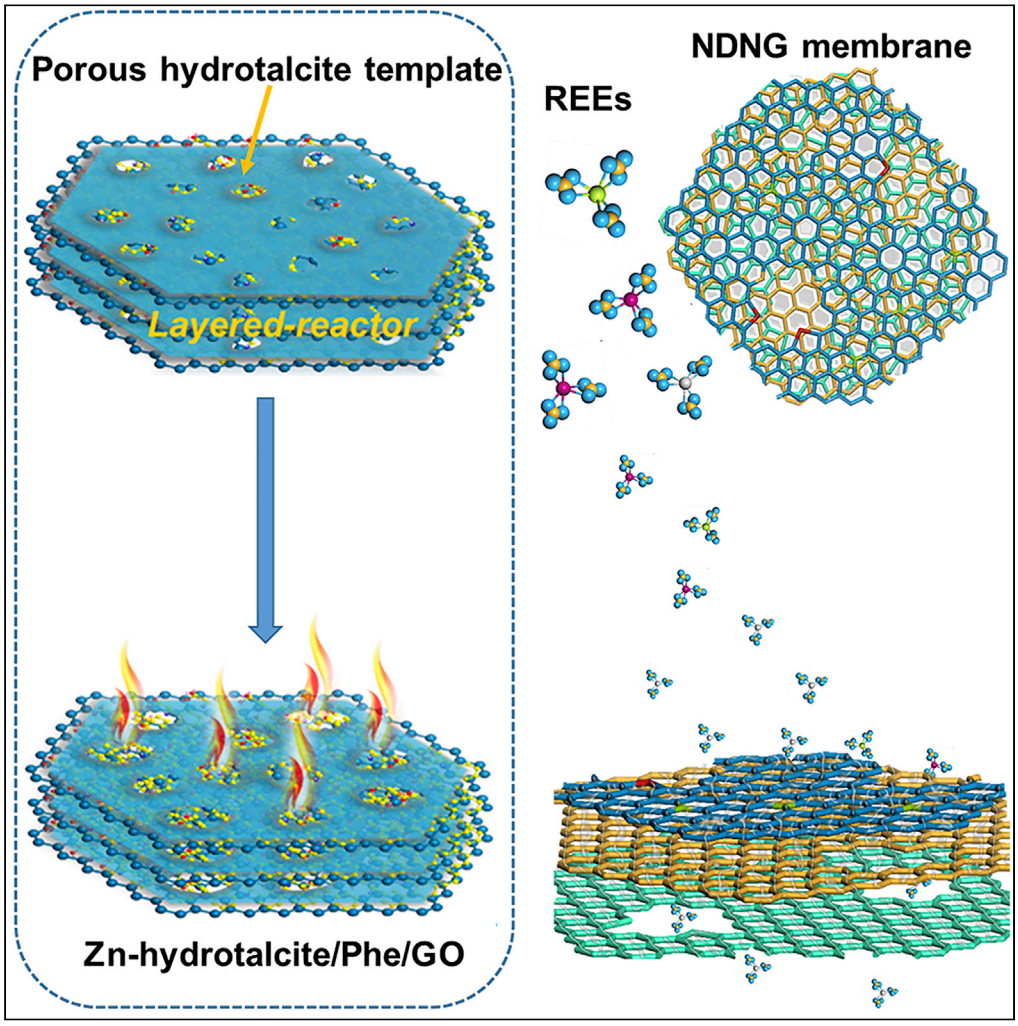

Hongxin Tan, Xin Zhang, Zhan Li, ..., Jia Chen, Juewen Liu, Hongdeng Qiu

lizhancg@licp.cas.cn (Z.L.)
hdqiu@licp.cas.cn (H.Q.)

HIGHLIGHTS

A multiple confinement strategy is constructed to achieve the synthesis of NDNG

Planar nitrogen-doped NDNG with tunable pore size is obtained by one-step synthesis

NDNG membrane presents excellent selectivity for rare earth in strong acidic media

Tan et al., iScience *24*, 101920
January 22, 2021
https://doi.org/10.1016/j.isci.2020.101920

iScience

CellPress
OPEN ACCESS

Article

Nitrogen-doped nanoporous graphene induced by a multiple confinement strategy for membrane separation of rare earth

Hongxin Tan,[1,5] Xin Zhang,[2] Zhan Li,[1,2,*] Qing Liang,[1] Jinsheng Wu,[3] Yanli Yuan,[3] Shiwei Cao,[4] Jia Chen,[1] Juewen Liu,[6] and Hongdeng Qiu[1,5,7,8,*]

Summary

Rare earth separation is still a major challenge in membrane science. Nitrogen-doped nanoporous graphene (NDNG) is a promising material for membrane separation, but it has not yet been tested for rare earth separation, and it is limited by multi-complex synthesis. Herein, we developed a one-step, facile, and scalable approach to synthesize NDNG with tunable pore size and controlled nitrogen content using confinement combustion. Nanoporous hydrotalcite from $Zn(NO_3)_2$ is formed between layers of graphene oxide (GO) absorbed with phenylalanine via confinement growth, thus preparing the sandwich hydrotalcite/phenylalanine/GO composites. Subsequently, area-confinement combustion of hydrotalcite nanopores is used to etch graphene nanopores, and the hydrotalcite interlayer as a closed flat nanoreactor induces two-dimensional space confinement doping of planar nitrogen into graphene. The membrane prepared by NDNG achieves separation of Sc^{3+} from the other rare earth ions with excellent selectivity (~3.7) through selective electrostatic interactions of pyrrolic-N, and separation selectivity of ~1.7 for Tm^{3+}/Sm^{3+}.

Introduction

Rare earth elements (REEs) are critical for designing optical, electrical, and magnetic functional materials because of their unique properties, which are therefore referred to as "industrial vitamin", and listed as strategic materials (Hu et al., 2018). REEs are very similar in their physicochemical properties, and exist in the form of associated ore deposits, suggesting that the separation and purification of individual REEs are necessary but extremely difficult (Cheisson and Schelter, 2019; Wang et al., 2018). The existing separation techniques of REEs involve cascade extraction (Brigham et al., 2017), chromatographic separation (Florek et al., 2016), and electrolytic separation technologies (Cheisson and Schelter, 2019) with the problems of complex operations, numerous procedures, high energy consumption, and low efficiency. In comparison, the membrane separation technology without phase change or additives has gained considerable attention owing to its simple, low carbon emission, easy operation, and suitable for industrial automation applications (Chen et al., 2017; Seo et al., 2018; Werber et al., 2016). However, it is still a challenge to use membrane technology for effective separation and purification of REEs because of the lack of appropriate materials (Chen et al., 2018).

The membrane of graphene oxide (GO) as a class of emerging membranes has been fabricated by stacking a large number of GO fragments with a controlled interlayer for precise ionic and molecular sieving (Chen et al., 2017; Huang et al., 2014; Joshi et al., 2014; Lipton et al., 2020). However, the low penetration rate of ions resulting from the limited interlayer spacing of GO membrane hinders the development in practical applications (Cohen-Tanugi and Grossman, 2012). As a very promising material, nitrogen-doped nanoporous graphene (NDNG) has attracted much attention (Ai et al., 2015; Bian et al., 2020; Li et al., 2017; Men et al., 2016; Pawlak et al., 2020; Sint et al., 2008; Wu et al., 2020; Yan et al., 2017). The presence of in-plane nanopores shortens the penetration path of ions to significantly enhance ion penetrability, and the incorporation of nitrogen into the graphene lattice enhances the electron-donor tendency of the nanoporous graphene for increasing separation selectivity toward ions. In addition, NDNG as carbon-based materials has high stability in strong acidic environments, thus it is expected to achieve the selective and efficient separation of REEs through NDNG membranes.

[1]CAS Key Laboratory of Chemistry of Northwestern Plant Resources and Key Laboratory for Natural Medicine of Gansu Province, Lanzhou Institute of Chemical Physics, Chinese Academy of Sciences, Lanzhou 730000, China

[2]School of Nuclear Science and Technology, Lanzhou University, Lanzhou 730000, China

[3]Lanzhou Ecology and Environment Monitoring Center of Gansu Province, Lanzhou 730000, China

[4]Institute of Modern Physics, Chinese Academy of Sciences, Lanzhou 730000, China

[5]University of Chinese Academy of Sciences, Chinese Academy of Sciences, Beijing 100049, China

[6]Department of Chemistry, Waterloo Institute for Nanotechnology, University of Waterloo, Waterloo, ON N2L 3G1, Canada

[7]College of Chemistry, Zhengzhou University, Zhengzhou 450001, China

[8]Lead contact

*Correspondence: lizhancg@licp.cas.cn (Z.L.), hdqiu@licp.cas.cn (H.Q.)

https://doi.org/10.1016/j.isci.2020.101920

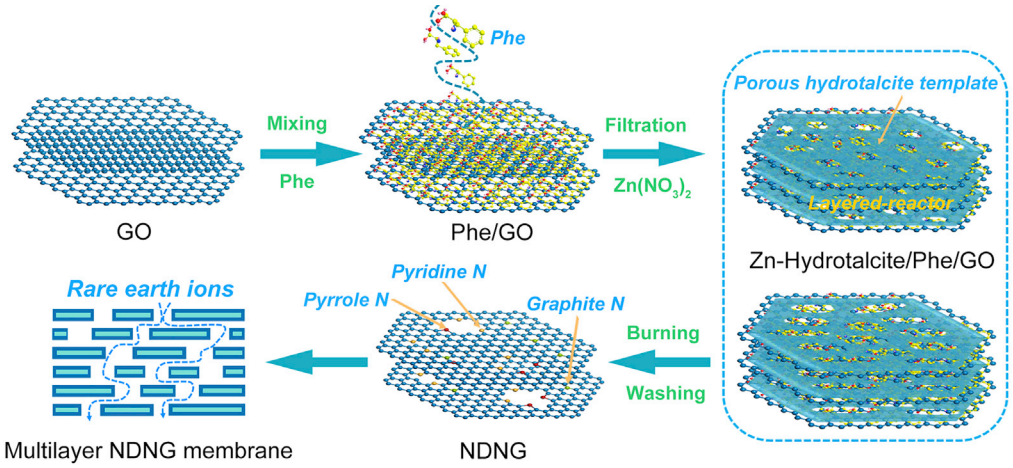

Scheme 1. Synthesis of NDNG through multiple confinement strategy and then NDNG membrane was prepared for rare earth elements separation

The synthesis technologies of NDNG from GO usually involve two independent steps (Bian et al., 2020; Men et al., 2016; Wu et al., 2020). The first step is the physical or chemical pore-making process with high energy-consuming and complex pre-preparation of the template, and the second step is a complex and long chemical doping process in a high-temperature sealed system. Unfortunately, the existing technologies of making pores are difficult to integrate with heteroatom doping for achieving a one-step synthesis of NDNG. Thus, the production of NDNG still suffers from complexity, low efficiency, and time-consuming, and it remains challenging until today.

In this work, we developed a new one-step combustion approach through a multiple confinement strategy to prepare NDNG with high separation selectivity toward REEs. Interlayer space of multilayer GO membrane was used for confined growth of Zn-hydrotalcite to construct sandwich composites of hydrotalcite/phenylalanine/GO. Nitrogen atoms from phenylalanine (Phe) were then doped into the graphene lattice between layers of Zn-hydrotalcite through the two-dimensional (2D) space confinement combustion, and the as-formed porous Zn-hydrotalcite was also used as a template to etch nanopores on GO via pore-area confinement combustion. NDNG with a large amount of planar nitrogen and tunable pore size was prepared as a membrane for REEs separation, and showed excellent selectivity. This discovery not only establishes a new route to prepare the heteroatom-doped nanoporous graphene, but also opens a new avenue for realizing high-performance REEs separation membranes.

Results and discussion

Design and synthesis of NDNG

The procedure for the synthesis of NDNG is illustrated in Scheme 1. Phe, as an aromatic and natural amino acid, is low cost and easily absorbed by GO via π–π stacking interaction (Ahn et al., 2014; Wang et al., 2014), thus it was selected to be the nitrogen doping precursor. As described in Scheme 1, after mixing uniformly of GO and Phe, the Phe molecules with benzene ring were basically parallel to the GO sheets forming well-ordered molecular films by filtering with filter paper (Krebs et al., 2018). Simultaneously, $Zn(NO_3)_2$ and H_2O were intercalated into the layers of as-formed Phe/GO membrane, which caused the 2D-space confinement self-controlled growth of Zn-hydrotalcite, and thus a sandwich composite of Zn-hydrotalcite/Phe/GO was prepared successfully. After burning and washing, NDNG with controllable pore size and nitrogen doping content can be obtained. More experiment details can be found in Supporting Information.

In order to confirm the formation of Zn-hydrotalcite/Phe/GO composites, the reaction process before combustion synthesis was monitored by X-ray diffraction (XRD). As shown in Figure 1A, the peak at ~10.7° is of (001) reflection of GO sheets, which is corresponding to the interplanar spacing of 8.3 Å, and the peaks at ~15°, 16.5°, 22.7°, and 34.2° are from the filter paper (Tan et al., 2020b). As compared to GO sheets, the (001) diffraction peak of GO in composites of Phe/GO and $Zn(NO_3)_2$/Phe/GO has shifted to smaller angles ~10.1° and 7.6°, and corresponding interlayer spacing increases to ~8.8 Å and 11.5 Å, respectively

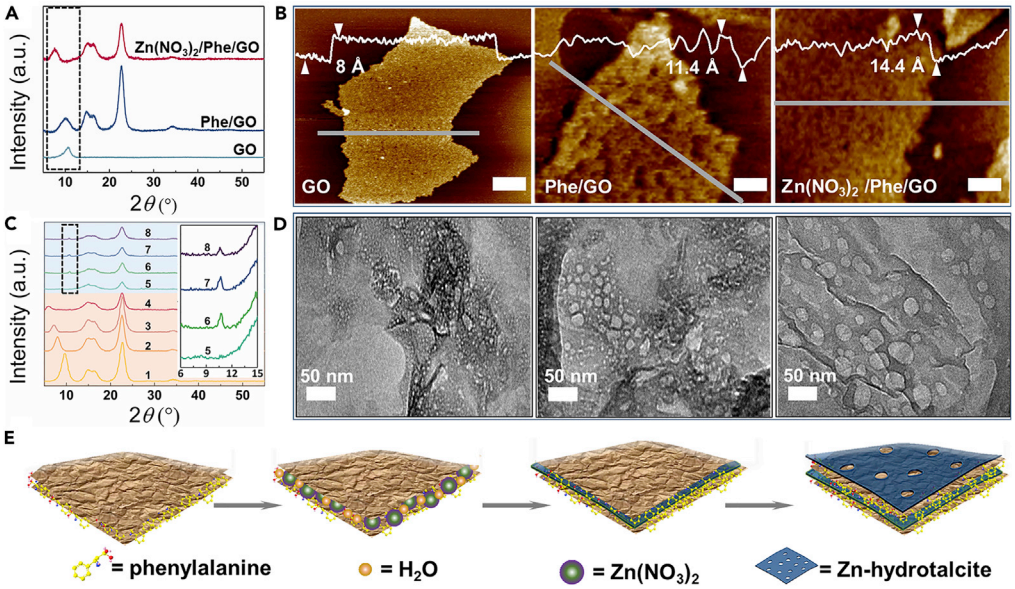

Figure 1. Fabricating mechanism of Zn-hydrotalcite/Phe/GO composites with sandwich structure

(A) XRD patterns of GO and GO composites with filter paper. The 2θ range for the (001) peak of the GO is highlighted in the dashed box.

(B) AFM images of GO nanosheet and GO composites samples. Scale bars are all 100 nm.

(C) XRD patterns of the composites $Zn(NO_3)_2$/Phe/GO at concentrations of $Zn(NO_3)_2$ = 50 g/L, 100 g/L, 150 g/L, 200 g/L, 300 g/L, 400 g/L, 450 g/L and 500 g/L (1–8), respectively. Insert: The X axis expansions in the 6–15° 2θ diffraction angle regions in the dashed box (5–8).

(D) TEM images of the composites $Zn(NO_3)_2$/Phe/GO at concentrations of $Zn(NO_3)_2$ = 200 g/L, 400 g/L, and 500 g/L from left to right, respectively.

(E) Schematic showing the formation of sandwich composites of Zn-hydrotalcite/Phe/GO.

(Figure S1A). Therefore, Phe and $Zn(NO_3)_2$ have been successfully inserted into the layers of GO, which causes an increase of the interplanar spacing of GO. The corresponding morphological information was obtained by atomic force microscopy (AFM), as shown in Figure 1B. AFM image of GO shows an unfolding 2D nanosheet, and the thickness of ~8 Å is consistent with that of monolayer GO (Xu et al., 2010). Moreover, the thickness of the composites Phe/GO and $Zn(NO_3)_2$/Phe/GO is 11.4 Å and 14.4 Å, respectively. The increased thickness of ~3.4 Å and 6.4 Å can result from the adsorption of Phe and $Zn(NO_3)_2$/Phe onto both sides of GO, respectively. Moreover, the uneven surface of the composites Phe/GO and $Zn(NO_3)_2$/Phe/GO with many nanopores can be observed clearly, which indicates that Phe and $Zn(NO_3)_2$ are not uniformly and completely covered on the GO basal plane but forming 2D porous layers. Thus the $Zn(NO_3)_2$/Phe/GO composite with sandwich structure was constructed successfully. For studying the forming process and structure of porous layers on the GO sheets, we analyzed XRD patterns of the samples $Zn(NO_3)_2$/Phe/GO prepared with different concentrations of $Zn(NO_3)_2$ as shown in Figure 1C. With the concentration of $Zn(NO_3)_2$ increasing from 50 to 200 g/L, the peak position of the (001) plane is shifted gradually to the low 2θ value from 9.6° to 5.7°, which corresponds to the increase of interlayer distance of GO from 9.2 to 15.4 Å caused by simultaneous intercalation of Phe and $Zn(NO_3)_2$ (Figure S1B). Meanwhile, the diffraction peak intensity of the (001) plane gradually decreases and the breadth of the peak increases with the increasing of the amount of $Zn(NO_3)_2$ in the hybrids, indicating an increase of the amorphous phase content.

The original GO peak completely disappears at the $Zn(NO_3)_2$ concentration of 300 g/L, meaning that the GO layers are fully intercalated with Phe and $Zn(NO_3)_2$, and the intercalated structure is no longer orderly arranged (Dimiev and Tour, 2014). Meanwhile, the new signal appears at 10.6° 2θ corresponding to an interlayer distance of 8.4 Å in the sample, which is indicative of the formation of a new crystalline phase. According to the previous report, the characteristic peak of the new phase can be indexed to the (003) plane of hydrotalcite (Garcia-Gallastegui et al., 2012), which we define as Zn-hydrotalcite covering GO. In the previous work, theoretical calculation showed that a cyclic structure can be formed between nitrate ions and water molecules by hydrogen bonding (Li et al., 2018). This distribution pattern leads to the formation of a

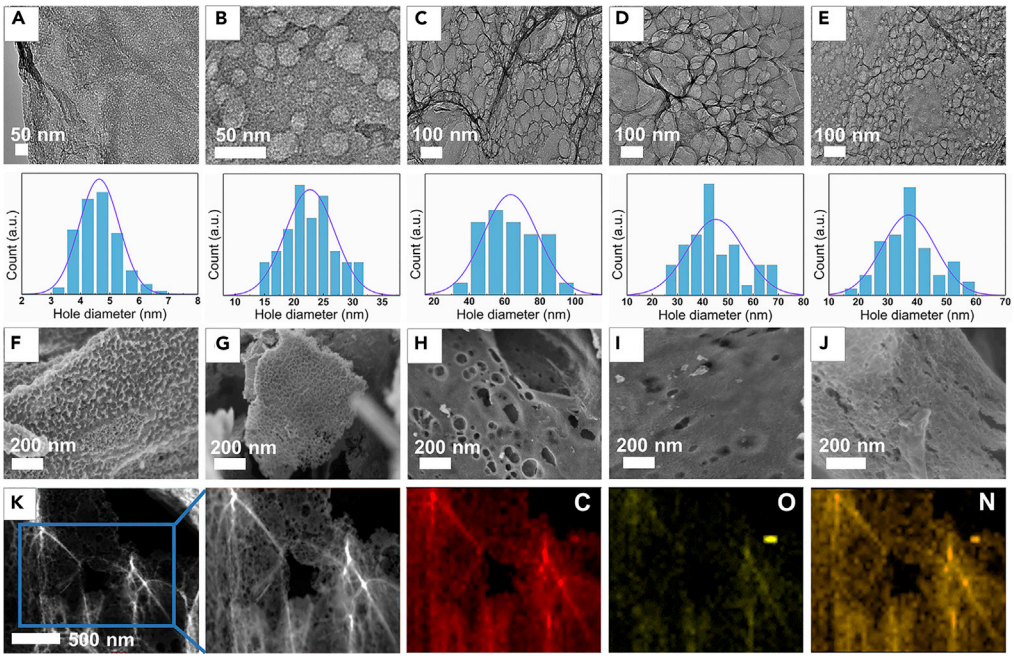

Figure 2. TEM and SEM images of NDNG

(A–J) TEM (A–E) and SEM (F–J) images of various NDNG prepared by different concentration of $Zn(NO_3)_2$ and Phe. (A, F) NDNG-1 ($Zn(NO_3)_2$: 200 g/L; Phe: 15 g/L). (B, G) NDNG-2 ($Zn(NO_3)_2$: 400 g/L; Phe: 15 g/L). (C, H) NDNG-3 ($Zn(NO_3)_2$: 500 g/L; Phe: 15 g/L). (D, I) NDNG-4 ($Zn(NO_3)_2$: 500 g/L; Phe: 10 g/L). (E, J) NDNG-5 ($Zn(NO_3)_2$: 500 g/L; Phe: 5 g/L).
(K) TEM image of NDNG-3 combined with EDS mapping in the same area and relative intensities of C (red), O (yellow), and N (orange) elements.

layered structure of ions and water molecules parallel to the graphene surface. After filtration, the layered structure can be remained between the graphene sheets. Algara-Siller et al. reported that the pressure between graphene layers is up to 1 GPa, which can induce graphene interlaminar water to become 2D ice (Algara-Siller et al., 2015). Thus, it can be inferred that the formation of Zn-hydrotalcite between GO layers can also be attributed to the high press. Most notably, the Zn-hydrotalcite structure formed in the GO interlayer galleries Inherits the ordered stacking of constituent graphene layers. Therefore, the stacking Zn-hydrotalcite/Phe/GO composite with sandwich structure is also confirmed by XRD patterns. With the increase of the amount of $Zn(NO_3)_2$ from 300 g/L to 500 g/L, the peak position remains unchanged but its intensity shows a trend from rising to decline, reaching the highest point at 400 g/L. The effect may be attributed to an increase in the integral lateral area of hydrotalcite, and then a mass of emerging pores on the Zn-hydrotalcite surface reduces its crystallinity (Garcia-Gallastegui et al., 2012; Li et al., 2018). These results also can be confirmed by transmission electron microscope (TEM) images as shown in Figures 1D and S2. First, with the increase of the amount of $Zn(NO_3)_2$ from 0 to 100 g/L, black covering on GO gradually deepens, and transparency of composite $Zn(NO_3)_2$/Phe/GO reduces. Then, some defective pores covering the GO surface can be observed at the amount of $Zn(NO_3)_2$ of 150 g/L (Figure S2). As shown in Figure 1D, the pore size on the surface of composites was easily regulated from small to large by increasing the concentration of $Zn(NO_3)_2$ from 200 g/L to 500 g/L. The results also show that the lateral size of the Zn-hydrotalcite depends on the salt concentration on the surface of Phe/GO after filtering. Therefore, there are many nanopores with tunable size on the surface of layered Zn-hydrotalcite, which can be used as nanotemplate for making pore through combustion etching. Meanwhile, a closed 2D interlayer nanospace between the layered Zn-hydrotalcites acts as nanoreactors to incorporate nitrogen from Phe into the graphene lattice to prepare NDNG (Figure 1E).

Morphological and structural characterizations

The pore size of the membrane and nitrogen content may be the key factors affecting the permeation and separation of REEs. Therefore, the concentration of $Zn(NO_3)_2$ in the reactant was adjusted to be 200, 400, and 500 g/L for controlling the pore size of NDNG to obtain NPNG-1, 2, and 3, respectively. Subsequently,

the adding amount of Phe is decreased from 15 g/L to 10 g/L and 5 g/L for obtaining NPNG-3, 4, and 5, respectively. After combustion treatment and washing, NDNG with different pore size and nitrogen content can be obtained as shown in Figure 2. The samples of NDNG-1, 2, and 3 show an average pore size of ~5, ~23, and ~65 nm, respectively (Figures 2A–2C, 2F-H), and the samples of NDNG-3, 4, and 5 exhibit the similar pore size (Figures 2C–2E, 2H-J). Thereby, it can be known that the morphology and size of pores on NDNG are dependent only on the addition amount of $Zn(NO_3)_2$. The element distribution of NPNG was performed by TEM with the corresponding EDS mappings. As shown in Figure 2K, N atoms are distributed uniformly and well-doped on the base plane, and around the pores of NDNG. In addition, the distribution intensity of O mappings is much lower than C and N, indicating that O atoms may be replaced with N atoms, or pyrolyzed during combustion. For all the NDNG samples, the XRD pattern undergoes significant changes as compared with pre-combustion composites (Figure S3). Only one broad pattern appears at $2\theta = 26^{\circ}$, which is corresponding to the interlayer distance of 3.4 Å originating from the (002) plane of reduced GO (Du et al., 2015; Song et al., 2019). These results also agree with the above element distribution that most oxygen-functional groups were replaced and removed after burning. Raman spectra in Figure S4 is used to provide the additional structural information. Two peaks can be observed at ~1335 cm^{-1} and 1596 cm^{-1}, which are corresponding to the D band and G band in the graphene, respectively. The intensity ratio of D band to G band (I_D/I_G) can be used to characterize the disorder degree (Lin et al., 2012; Tan et al., 2020a). Apparently, a clear increase of I_D/I_G from NDNG-1 to NDNG-3 can be found from 0.97 to 1.30 with the increase of the pore size, which is consistent with previous reports (Zhou et al., 2014). Moreover, I_D/I_G ratios decrease slightly from 1.30 to 1.10 for NDNG-3 and NDNG-5, indicating that the incorporation of N atoms into the graphene carbon framework can increase the defective degree of NDNG (Lin et al., 2012). In order to evaluate the accessible surface of NDNG, N_2 adsorption-desorption isotherms are recorded in Figure S5. The Brunauer-Emmett-Teller surface area of NDNG-1, 2, and 3 is ~352, 579, and 586 m^2/g, respectively (Figure S5A). Therefore, the specific surface area of NDNG increases with the increase of pore size, which indicates that the resulting pore can improve significantly the accessible surface. As can be seen from Figure S5B, the specific surface area of NDNG-3, 4, and 5 is ~586, 501, and 500 m^2/g, respectively, suggesting that the introduction of nitrogen atoms increases slightly the surface area of NDNG. Fourier transform infrared (FT-IR) spectroscopy and thermogravimetric analysis (TGA) of different samples including GO, Phe/GO, Zn-hydrotalcite/Phe/GO and NDNG-3 also show that NDNG was prepared successfully (Figures S6 and S7).

The elemental composition and bonding configurations of NDNG are characterized by X-ray photoelectron spectrometer (XPS) as shown in Figure 3. From XPS spectra (Figure 3A), it can be found that the major component in the as-prepared samples is C (284.6 eV) and followed by heteroatoms including N (397.1–402.9 eV) and O (530–534 eV). The nitrogen doping content significantly decreases from 4.2% for NDNG-3 to 3.3% for NDNG-4, and to 2.9% for NDNG-5, which indicates that the nitrogen content of NDNG can be controlled by adjusting the addition amount of Phe. As shown in Figure S8, the C 1s spectrum is deconvoluted into four peaks at 284.8, 285.5, 286.5, and 288 eV, corresponding to C-C, C=N/C-O, C-N/C=O, and O-C=O, respectively (Lin et al., 2012). The presence of C-N or C=N bond further confirms the formation of the N-doped graphite structure of the prepared samples. The high-resolution spectrum of N 1s for NDNG could be deconvoluted into three peaks at 398.5 eV, 400 eV, and 401.2 eV, which correspond to pyridinic (N6), pyrrolic (N5), and quaternary nitrogen (NQ) (Men et al., 2016), respectively (Figures 3B–3F). N6 and N5 are considered as planar sp^2 hybridized nitrogen, and NQ is thought to be tetrahedral sp^3 hybridized nitrogen (Figure 3G) (Ding et al., 2013). After combustion treatment, NQ species only accounts for 5.8, 3.7, 7.1, 5.5, and 5.9% of the N species in NDNG-1, NDNG-2, NDNG-3, NDNG-4, and NDNG-5, respectively. It is worth noting that NDNG-2 is doped with a high planar-nitrogen content of 96.3%. These results can be attributed to the space-confinement doping of nitrogen between the Zn-hydrotalcite 2D layers, especially resulting from the largest crystallite size of the Zn-hydrotalcite with $Zn(NO_3)_2$ concentration of 400 g/L. Therefore, it can be inferred that nitrogen doping of GO caused by nanospace-confinement from Zn-hydrotalcite can selectively produce planar N6 and N5 in NDNG and constrains the formation of NQ dopant via steric hindrance effect, which is very corresponding with the previously reported mechanism (Ding et al., 2013). For comparison, alanine (Ala) was chosen as another kind of nitrogen doping agent, which is similar to Phe but without the phenyl ring in chemical structure. As shown in Table S1, the combustion products obtained with different adding order of amino acid and salt into GO suspension exhibit different N doping amount in the approximate order: $Zn(NO_3)_2$/Phe/GO > Phe/$Zn(NO_3)_2$/GO > $Zn(NO_3)_2$/Ala/GO > Ala/$Zn(NO_3)_2$/GO. The higher N doping amount of NDNG prepared by Phe may result from a higher adsorption amount of Phe adsorbed on the GO surface, meaning that the

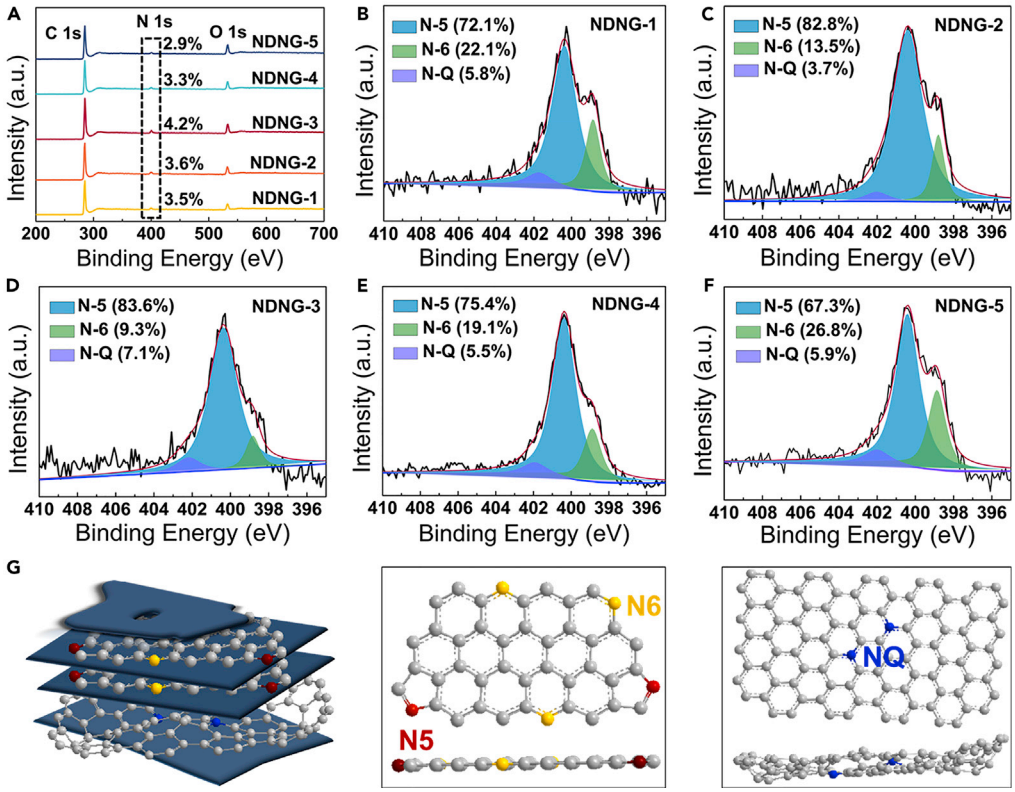

Figure 3. XPS spectrum of NDNG

(A) Survey spectrum of NDNG.

(B–F) Typical high-resolution XPS N 1s spectra of NDNG.

(G) Schematic representation showing the selectivity for planar N during NDNG synthesis.

interaction between GO and aromatic Phe is stronger than that between GO and non-aromatic Ala. Moreover, the N doping amount of NDNG prepared by $Zn(NO_3)_2$/amino acid/GO adding order is higher than the one prepared by amino acid/$Zn(NO_3)_2$/GO, suggesting that the adding order also could affect the N doping content of NDNG. According to the above confinement combustion mechanism, only amino acid molecules between Zn-hydrotalcite layers can be mostly incorporated into the graphene lattice. Therefore, as compared to the addition of $Zn(NO_3)_2$ before amino acids into GO suspension, the addition of amino acids before $Zn(NO_3)_2$ can cause more amino acid molecules to be sandwiched between layers of Zn-hydrotalcite after filtering and drying, thereby synthesizing NDNG with higher nitrogen doping amount after burning, and this also means that nitrogen loss during combustion can be alleviated by the formation of Zn-hydrotalcite.

Separation of REEs

Currently, membrane strategies for REEs separation are mainly classified into two types: liquid membranes and solid membranes (Chen et al., 2018). During the last few decades, liquid membranes demonstrate efficient permeation and separation performances toward metal ions on account of its large mass transfer interfacial areas (Anitha et al., 2013; Kim et al., 2016; Pei et al., 2011), but it got no breakthrough in scale-up experiments due to poor stability. In this regard, solid membranes are more promising because the solid ones are more stable, and suitable for industrial applications (Chen et al., 2018). The current interests in solid membrane technique for REEs separation are mainly in polymer inclusion membranes and some ion imprinted techniques on polymeric membranes (Croft et al., 2018; Hong et al., 2014; Yusoff et al., 2017; Zheng et al., 2017). However, the major problem with most polymer-based solid membranes is the weak stability and susceptibility in a concentrated acid environment of REEs hydrometallurgy process. Considering the separation nature of membranes, the high porosity, surface area and the abundance of surface nitrogen atoms of the NDNG inspired us to solve a longstanding problem of REEs separation in strong acidic media.

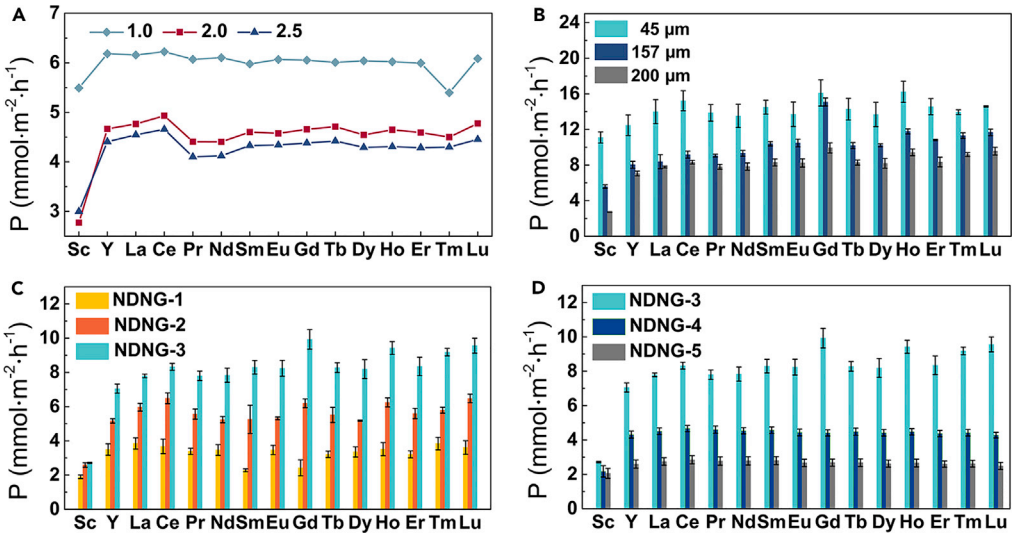

Figure 4. Permeation and separation of REEs through NDNG membranes

(A) Effect of pH on the separation for NDNG-1 membrane. The pH of feed solution of REEs (5 mM) was adjusted to 3.0. The pH of driven solution was adjusted by diluted NH_4OH or HNO_3 solution. The thickness of the membranes is 105 μm.

(B) Permeation flux of REEs as a function of the NDNG-1 membrane thickness. The feed solution has a concentration of 5 mM for all elements at a pH of 3.0; The driven solution is dilute nitric acid at a pH of 2.0.

(C and D) Permeance with different NDNG membranes (NDNG-1, NDNG-2, NDNG-3, NDNG-4, and NDNG-5) for the REEs. The feed solution has a concentration of 5 mM for all elements at a pH of 3.0; The driven solution is dilute nitric acid at a pH of 2.0. The thickness of the membranes is 105 μm.

The resulting NDNG-1, NDNG-2, NDNG-3, NDNG-4, and NDNG-5 were prepared as membrane by vacuum filtration for studying its separation selectivity toward REEs. As shown in Figures S9A–S9E, the uniform surfaces of the membranes can be clearly observed. The scanning electron microscope (SEM) characterizations of the cross-section morphology of the membranes are shown in Figures S9F–S9J, which reveal that the as-prepared NDNG membranes possess a lamellar structure. Subsequently, the test membranes were fixed between the feed and driven tanks for performing a series of ion-penetration experiments in Figure S9K. Because industrial processes involving REEs separation are likely to be conducted in acidic conditions (Wang et al., 2018), a pH of 3 was selected in the feed solution for all experiments unless otherwise stated. As shown in Figure S10, the concentration of REEs (Sc^{3+} and Gd^{3+}) in the driven solution increases significantly in a near-linear manner over time. The NDNG membrane still maintains higher selectivity for REEs (Sc^{3+} and Gd^{3+}) after separation for 48 hr, which indicates that the separation performance of membrane is stable under the filtration conditions. The Gd^{3+} permeates efficiently through the NDNG-1 membrane, whereas Sc^{3+} infiltrates much more slowly. Subsequently, the penetration and selectivity capacity of the NDNG-1 membrane were evaluated in a series of driven solutions with different pH values. According to previous reports, REEs begin to precipitate as hydroxides out of solution at pH > 4 (Giret et al., 2018; Wang et al., 2018). As shown in Figure 4A, in the effective range (pH < 3), a high concentration of H^+ in the driven solution could promote significantly the permeation of REEs through NDNG-1 membrane, indicating ion exchange during the separation process (Li et al., 2016). The lowest infiltration concentration of Sc^{3+} was achieved at a pH of 2.0 of the driven solution, and the highest separation factor can be obtained between Sc^{3+} and other REEs, meaning that pH can be a controllable parameter to improve the permeation selectivity of NDNG for REEs. In order to further explore the effect of NDNG on the separation of the REEs, we assessed the permeation properties of NDNG membranes with different thicknesses. As shown in Figure 4B, the flux of the REEs always reduces with the increasing membrane thickness, which could be ascribed to a growth in the diffusion hamper or resistance properties of membranes (Fang et al., 2016; Meng et al., 2017). Here, the maximal separation factor increased from 1.5 to 2.9 with the increase of the thickness of NDNG-1 membranes (Figure S11), which can be attributed to the increased interaction sites (Huang et al., 2013). In addition, a huge difference can be found in the permeation ability of different NDNG membranes in the sequence NDNG-3 > NDNG-2 > NDNG-1 (Figure 4C), which can be ascribed to the increase of pore size of NDNG. The selective separation behavior of Sc^{3+} from other REEs through the NDNG membrane is investigated in Figure S12A. Interestingly, the separation factor

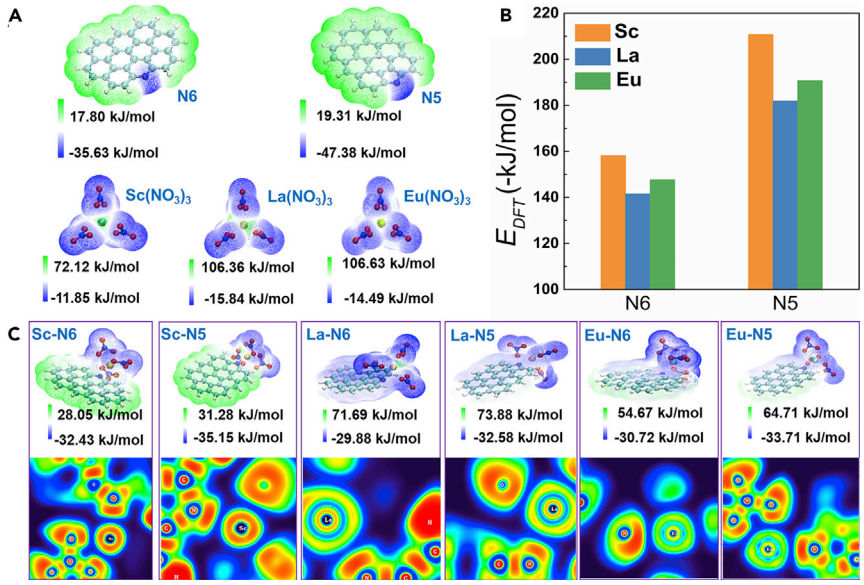

Figure 5. Theoretical computations of the interaction energy between REEs and NDNG

(A) The most stable optimized geometries and the corresponding electrostatic potential surfaces of N6 and N5 on the sheets of NDNG and nitrate of Sc, La, Eu. The purple region represents negative ESP, while the green region represents positive ESP.

(B) Comparison of the interaction energies of the REEs (Sc, La, Eu) with N6 and N5.

(C) Upper panel: the most stable optimized geometries and the corresponding electrostatic potential surfaces of the complexes of REEs with N6 and N5 along with their interaction energies, respectively, where the cations are Sc^{3+}, La^{3+}, and Eu^{3+}. Lower panel: corresponding color-filled maps of electron location function.

of M/Sc increases with the increase of pore size, and the largest separation factor is about 3.7 corresponding to Gd^{3+}/Sc^{3+}. As shown in Table S2, the separation performance of the NDNG membrane is very similar to that of ion imprinted membranes (Cui et al., 2019; Li et al., 2015; Liu et al., 2014, 2017; Lu et al., 2018; Zheng et al., 2017, 2018). Because of the large pores in NDNG-3 (~65 nm), the selectivity for Sc^{3+} from other REEs cannot be attributed to the special pore structure and ionic-radius-based theories (Sun et al., 2013). It is therefore inferred that the electrostatic attractions and chemical interactions between functional groups of NDNG sheets and hydrated ions may be responsible for the selectivity of membranes toward REEs. Based on the above XPS analysis, combining high permeability and high selectivity of NDNG-3 membrane to REEs may be attributed to the highest percentage of N5 in N species in NDNG-3 (>83%). As shown in Figures 4D and S12B, both permeation ability and selectivity decrease with a decrease in the N-doping content of NDNG, indicating that the doping of nitrogen atoms has an important impact on the separation of REEs. Further analysis revealed in Figure S13 shows that NDNG-3 could also be used to achieve the selective separation between lanthanide elements. The highest selectivity is calculated as ~1.7 corresponding to Tm^{3+}/Sm^{3+}. As we know, the long-term stability of membranes is critically important for industrial applications (Thebo et al., 2018). Compared with liquid membranes (Chen et al., 2018), the NDNG membranes are very stable and remain their original structure in acidic (pH = 3.0) solutions even after 90 days (Figure S14). In short, the NDNG membrane with high permeation and separation ability and strong acid-resistant ability has great potential in application.

Theoretical simulation

Finally, the density functional theory (DFT) calculations were further performed to illustrate the underlying mechanism taking place during the ion transportation and separation process. According to our XPS results, the N configuration in the as-prepared NDNG is dominated by N6 and N5. Therefore, the electrostatic potential (ESP) on van der Waals surface is calculated of N6 and N5 on the sheets of NDNG and nitrate of Sc, La, Eu, respectively. Figure 5A shows that the site of N5 possesses a more negative ESP than that of N6, which indicates that N5 has a stronger ability to attract REEs by electrostatic force. Subsequently, the DFT electronic energy (E_{DFT}) was calculated to illustrate the interactions between cations and two types of

planar nitrogen atoms. It is apparent that for all the complex systems, the N5 presents a stronger binding energy with three metal ions (from ~-211 to ~ -191 kJ/mol) than N6 (from ~-158 to ~ -148 kJ/mol), which confirms that the N5 plays a leading role in the process of separation in this work. More importantly, it is calculated that the interaction energies of Sc^{3+} ion both on N6 and N5 are more negative relative to La^{3+} and Eu^{3+} (Figure 5B), which can be used to explain the flux of Sc^{3+} is always lower than that of the other REEs. In addition, to further give a clear and quantitative description of the feasible chemical bond between ions and N atoms, electron location function analysis was used in this work. Figure 5C shows that the interactions between the ions and N atoms are mainly electrostatic interactions without the formation of chemical bonds. Therefore, the strength of electrostatic interactions plays a decisive role in defining the ultimate separation performances. As far as the transport properties are concerned, solid membranes commonly present two kinds of transport mechanisms: facilitated and retarded transport (Chen et al., 2018). In order to exclude the adsorption effect, the maximum adsorption capacity for NDNG-3 was calculated from adsorption isotherm experiments at pH 3. For Sc^{3+}, the equilibrium isotherm was established and fitted well with Langmuir model as shown in Figure S15. The parameters of the corresponding linear regressions are summarized in Table S3. The Freundlich model was also used but did not fit to the experimental isotherm data. The experimental maximum adsorption capacity of NDNG-3 for Sc^{3+} is calculated to be 1.44 mg/g in the presence of all other REEs at the same concentration. The concentration corresponding to the maximum adsorption capacity is considerably lower than the concentration of the feed solution (5 mM). Therefore, the rejection of the membrane toward Sc^{3+} is not due to the adsorption of ions to NDNG in this work.

Conclusions

In summary, we have developed a one-step route for synthesizing nitrogen-doped nanopores graphene and clarified clearly the mechanism of multiple confinement combustion strategy. Because of steric hindrance resulting from interspace of formed Zn-hydrotalcite, planar N include pyrrolic-N and pyridinic-N were generated selectively in the flat 2D nanoreactor in combustion. Meanwhile, the N doping amount and pore size of the synthetic NDNG material can be tuned by adjusting the amount of amino acid and salt, respectively. The as-prepared NDNG membrane showed long-term stability and excellent separation performance toward REEs. Theoretical simulations also revealed that planar N, especially pyrrolic-N, served as selective adsorption sites during the separation process. Combining the simple and efficient preparation approach and excellent separation stability, we conclude that fabricating NDNG membranes is a promising membrane strategy for green separation of REEs. In addition, this novel synthetic method can be extended to the synthesis of other heteroatom-doped nanopores materials, which will have great potentials in not only the membrane separation field but also in other fields such as catalysis, sensors, and supercapacitors.

Limitations of the study

In addition to the NDNG being prepared in this study, more heteroatoms doping porous 2D materials can be prepared and applied for more potential breakthroughs in structure control and performance enhancement.

Resource availability

Lead contact

Hongdeng Qiu (hdqiu@licp.cas.cn) serves as the lead contact.

Materials availability

No new unique reagents were generated.

Data and code availability

Data supporting the main conclusions of this study are available from the corresponding author upon request.

Methods

All methods can be found in the accompanying Transparent Methods supplemental file.

Supplemental information

Supplemental Information can be found online at https://doi.org/10.1016/j.isci.2020.101920.

Acknowledgments

This work was supported by the National Key R&D Program of China (2019YFC1905501), the National Natural Science Foundation of China (No. 21974146, 21822407, 21675164), CAS "Light of West China" Program and the Foundation for Sci & Tech Research Project of Gansu Province (18JR3RA387).

Author contributions

H.T., Z.L., and H.Q. conceived the project. Z.L. and H.Q. supervised the project. H.T. and Z.L. performed the experiments and characterizations. X.Z. and S.C. carried out the theoretical simulations and analysis. H.T., Z.L., and Q.L. carried out AFM testing and analyzed the data. H.T., J.W., and Y.Y. analyzed the ICP-MS data. H.T., Z.L., J. C. and H.Q. co-wrote the manuscript. All authors discussed the results and commented on the manuscript.

Declaration of interests

A China patent application (202010861481.0) has been filed, with H.Q., H.T., Z.L., and J.C. as inventors, covering the method for fabricating nitrogen-doped nanoporous graphene membranes described herein. The authors declare no competing interests.

Received: September 26, 2020
Revised: November 24, 2020
Accepted: December 4, 2020
Published: January 22, 2021

References

Ahn, H., Kim, T., Choi, H., Yoon, C., Um, K., Nam, J., Ahn, K.H., and Lee, K. (2014). Gelation of graphene oxides induced by different types of amino acids. Carbon *71*, 229–237.

Ai, W., Jiang, J., Zhu, J., Fan, Z., Wang, Y., Zhang, H., Huang, W., and Yu, T. (2015). Supramolecular polymerization promoted in situ fabrication of nitrogen-doped porous graphene sheets as anode materials for Li-Ion Batteries. Adv. Energy Mater. *5*, 1500559.

Algara-Siller, G., Lehtinen, O., Wang, F.C., Nair, R.R., Kaiser, U., Wu, H.A., Geim, A.K., and Grigorieva, I.V. (2015). Square ice in graphene nanocapillaries. Nature *519*, 443–445.

Anitha, M., Ambare, D.N., Kotekar, M.K., Singh, D.K., and Singh, H. (2013). Studies on Permeation of Nd (III) through supported liquid membrane using DNPPA plus TOPO as Carrier. Sep. Sci. Technol. *48*, 2196–2203.

Bian, Y., Wang, H., Hu, J., Liu, B., Liu, D., and Dai, L. (2020). Nitrogen-rich holey graphene for efficient oxygen reduction reaction. Carbon *162*, 66–73.

Brigham, D.M., Ivanov, A.S., Moyer, B.A., Delmau, L.H., Bryantsev, V.S., and Ellis, R.J. (2017). Trefoil-shaped outer-sphere ion clusters mediate lanthanide(III) ion transport with diglycolamide ligands. J. Am. Chem. Soc. *139*, 17350–17358.

Cheisson, T., and Schelter, E.J. (2019). Rare earth elements: mendeleev's bane, modern marvels. Science *363*, 489–493.

Chen, L., Shi, G., Shen, J., Peng, B., Zhang, B., Wang, Y., Bian, F., Wang, J., Li, D., Qian, Z., et al. (2017). Ion sieving in graphene oxide membranes via cationic control of interlayer spacing. Nature *550*, 415–418.

Chen, L., Wu, Y., Dong, H., Meng, M., Li, C., Yan, Y., and Chen, J. (2018). An overview on membrane strategies for rare earths extraction and separation. Sep. Purif. Technol. *197*, 70–85.

Cohen-Tanugi, D., and Grossman, J.C. (2012). Water desalination across nanoporous graphene. Nano Lett. *12*, 3602–3608.

Croft, C.F., Almeida, M., Cattrall, R.W., and Kolev, S.D. (2018). Separation of lanthanum(III), gadolinium(III) and ytterbium(III) from sulfuric acid solutions by using a polymer inclusion membrane. J. Membr. Sci. *545*, 259–265.

Cui, K., Gao, B., Tai, M., and Su, B. (2019). A facile bionic strategy towards Gd (III)-imprinted membranes via interlaced stacking of one-dimensional/two-dimensional nanocomposite materials. J. Taiwan Inst. Chem. Eng. *95*, 652–659.

Dimiev, A., and Tour, J. (2014). Mechanism of graphene oxide formation. ACS Nano *8*, 3060–3068.

Ding, W., Wei, Z., Chen, S., Qi, X., Yang, T., Hu, J., Wang, D., Wan, L.-J., Alvi, S., and Li, L. (2013). Space-confinement-Induced synthesis of pyridinic- and pyrrolic-nitrogen-doped graphene for the catalysis of oxygen reduction. Angew. Chem. Int. Ed. *52*, 11755–11759.

Du, D., Li, P., and Ouyang, J. (2015). Nitrogen-doped reduced graphene oxide prepared by simultaneous thermal reduction and nitrogen doping of graphene oxide in air and its application as an electrocatalyst. ACS Appl. Mater. Interfaces *7*, 26952–26958.

Fang, Q., Zhou, X., Deng, W., Zheng, Z., and Liu, Z. (2016). Freestanding bacterial cellulose-graphene oxide composite membranes with high mechanical strength for selective ion permeation. Sci. Rep. *6*, 33185.

Florek, J., Giret, S., Juere, E., Lariviere, D., and Kleitz, F. (2016). Functionalization of mesoporous materials for lanthanide and actinide extraction. Dalton Trans. *45*, 14832–14854.

Garcia-Gallastegui, A., Iruretagoyena, D., Gouvea, V., Mokhtar, M., Asiri, A.M., Basahel, S.N., Al-Thabaiti, S.A., Alyoubi, A.O., Chadwick, D., and Shaffer, M.S.P. (2012). Graphene oxide as support for layered double hydroxides: enhancing the CO_2 adsorption capacity. Chem. Mater. *24*, 4531–4539.

Giret, S., Hu, Y., Masoumifard, N., Boulanger, J.-F., Juere, E., Kleitz, F., and Lariyiere, D. (2018). Selective separation and preconcentration of scandium with mesoporous silica. ACS Appl. Mater. Interfaces *10*, 448–457.

Hong, G., Shen, L., Wang, M., Yang, Y., Wang, X., Zhu, M., and Hsiao, B. (2014). Nanofibrous polydopamine complex membranes for adsorption of Lanthanum (III) ions. Chem. Eng. J. *244*, 307–316.

Hu, Y., Florek, J., Lariviere, D., Fontaine, F.-G., and Kleitz, F. (2018). Recent advances in the separation of rare earth elements using mesoporous hybrid materials. Chem. Rec. *18*, 1261–1276.

Huang, H., Mao, Y., Ying, Y., Liu, Y., Sun, L., and Peng, X. (2013). Salt concentration, pH and pressure controlled separation of small molecules through lamellar graphene oxide membranes. Chem. Commun. (Camb.) *49*, 5963–5965.

Huang, K., Liu, G., Lou, Y., Dong, Z., Shen, J., and Jin, W. (2014). A graphene oxide membrane with highly selective molecular separation of aqueous organic solution. Angew. Chem. Int. Ed. *53*, 6929–6932.

Joshi, R.K., Carbone, P., Wang, F., Kravets, V.G., Su, Y., Grigorieva, I.V., Wu, H., Geim, A.K., and Nair, R.R. (2014). Precise and ultrafast molecular sieving through graphene oxide membranes. Science *343*, 752–754.

Kim, D., Powell, L., Delmau, L.H., Peterson, E.S., Herchenroeder, J., and Bhave, R.R. (2016). A supported liquid membrane system for the selective recovery of rare earth elements from neodymium-based permanent magnets. Sep. Sci. Technol. *51*, 1716–1726.

Krebs, E., Grabill, L., and Riemann, A. (2018). Amino acid nanopatterning on graphite. Surf. Sci. *678*, 143–148.

Li, J., Lin, L., Rui, D., Li, Q., Zhang, J., Kang, N., Zhang, Y., Peng, H., Liu, Z., and Xu, H. (2017). Electron hole symmetry breaking in charge transport in nitrogen-doped graphene. ACS Nano *11*, 4641–4650.

Li, K., Gao, Q., Yadavalli, G., Shen, X., Lei, H., Han, B., Xia, K., and Zhou, C. (2015). Selective adsorption of gd^{3+} on a magnetically retrievable imprinted chitosan/carbon nanotube composite with high capacity. ACS Appl. Mater. Interfaces *7*, 21047–21055.

Li, Z., Liu, Y., Zhao, Y., Zhang, X., Qian, L., Tian, L., Bai, J., Qi, W., Yao, H., Gao, B., et al. (2016). Selective separation of metal ions via monolayer nanoporous graphene with carboxyl groups. Anal. Chem. *88*, 10002–10010.

Li, Z., Zhang, X., Tan, H., Qi, W., Wang, L., Ali, M., Zhang, H., Chen, J., Hu, P., Fan, C., et al. (2018). Combustion fabrication of nanoporous graphene for ionic separation membranes. Adv. Funct. Mater. *28*, 1805026.

Lin, Z., Waller, G., Liu, Y., Liu, M., and Wong, C. (2012). Facile synthesis of nitrogen-doped graphene via pyrolysis of graphene oxide and urea, and its electrocatalytic activity toward the oxygen-reduction reaction. Adv. Energy Mater. *2*, 884–888.

Lipton, J., Weng, G.-M., Röhr, J.A., Wang, H., and Taylor, A.D. (2020). Layer-by-layer assembly of two-dimensional materials: meticulous control on the nanoscale. Matter *2*, 1148–1165.

Liu, E., Xu, X., Zheng, X., Zhang, F., Liu, E., and Li, C. (2017). An ion imprinted macroporous chitosan membrane for efficiently selective adsorption of dysprosium. Sep. Purif. Technol. *189*, 288–295.

Liu, Y., Tian, S., Meng, X., Dai, X., Liu, Z., Meng, M., Han, J., Wang, Y., Chen, R., Yan, Y., et al. (2014). Synthesis, characterization, and adsorption properties of a Ce(III)-imprinted polymer supported by mesoporous SBA-15 matrix by a surface molecular imprinting technique. Can. J. Chem. *92*, 257–266.

Lu, J., Wu, Y., Lin, X., Gao, J., Dong, H., Chen, L., Qin, Y., Wang, L., and Yan, Y. (2018). Anti-fouling and thermosensitive ion-imprinted nanocomposite membranes based on grapheme oxide and silicon dioxide for selectively separating europium ions. J. Hazard. Mater. *353*, 244–253.

Men, B., Sun, Y., Li, M., Hu, C., Zhang, M., Wang, L., Tang, Y., Chen, Y., Wan, P., and Pan, J. (2016). Hierarchical metal-free nitrogen-doped porous graphene/carbon composites as an efficient oxygen reduction reaction catalyst. ACS Appl. Mater. Inter. *8*, 1415–1423.

Meng, C., Sheng, Y., Chen, Q., Tan, H., and Liu, H. (2017). Exceptional chiral separation of amino acid modified graphene oxide membranes with high-flux. J. Membr. Sci. *526*, 25–31.

Pawlak, R., Liu, X., Ninova, S., D'Astolfo, P., Drechsel, C., Sangtarash, S., Häner, R., Decurtins, S., Sadeghi, H., Lambert, C.J., et al. (2020). Bottom-up synthesis of nitrogen-doped porous graphene nanoribbons. J. Am. Chem. Soc. *142*, 12568–12573.

Pei, L., Wang, L., and Yu, G. (2011). Separation of Eu(III) with supported dispersion liquid membrane system containing D2EHPA as carrier and HNO_3 solution as stripping solution. J. Rare Earths *29*, 7–14.

Seo, D.H., Pineda, S., Woo, Y.C., Xie, M., Murdock, A.T., Ang, E.Y.M., Jiao, Y., Park, M.J., Lim, S.I., Lawn, M., et al. (2018). Anti-fouling graphene-based membranes for effective water desalination. Nat. Commun. *9*, 683.

Sint, K., Wang, B., and Kral, P. (2008). Selective ion passage through functionalized graphene nanopores. J. Am. Chem. Soc. *130*, 16448–16449.

Song, L., Zhang, H., Cai, T., Chen, J., Li, Z., Guan, M., and Qiu, H. (2019). Porous graphene decorated silica as a new stationary phase for separation of sulfanilamide compounds in hydrophilic interaction chromatography. Chin. Chem. Lett. *30*, 863–866.

Sun, P., Zhu, M., Wang, K., Zhong, M., Wei, J., Wu, D., Xu, Z., and Zhu, H. (2013). Selective Ion penetration of graphene oxide membranes. ACS Nano *7*, 428–437.

Tan, H., Liu, T., Zhang, X., Shan, Q., Chen, J., Li, Z., Ihara, H., and Qiu, H. (2020a). Preparation of vortex porous graphene chiral membrane for enantioselective separation. Anal. Chem. *92*, 13630–13633.

Tan, H., Zhang, X., Li, Z., and Qiu, H. (2020b). Small-scale nanoparticles pyrolyzed from layered hydrotalcite between graphene interlayers as intermediates to self-assemble into metal oxide nanosheets and hollow nanospheres. Chem. Nano. Mat *6*, 1270–1275.

Thebo, K.H., Qian, X., Zhang, Q., Chen, L., Cheng, H.-M., and Ren, W. (2018). Highly stable graphene-oxide-based membranes with superior permeability. Nat. Commun. *9*, 1486.

Wang, T., Wang, L., Wu, D., Xia, W., Zhao, H., and Jia, D. (2014). Hydrothermal synthesis of nitrogen-doped graphene hydrogels using amino acids with different acidities as doping agents. J. Mater. Chem. A. *2*, 8352–8361.

Wang, Z., Brown, A.T., Tan, K., Chabal, Y.J., and Balkus, K.J., Jr. (2018). Selective extraction of thorium from rare earth elements using wrinkled mesoporous carbon. J. Am. Chem. Soc. *140*, 14735–14739.

Werber, J.R., Osuji, C.O., and Elimelech, M. (2016). Materials for next-generation desalination and water purification membranes. Nat. Rev. Mater. *1*, 16018.

Wu, D., Song, W., Chen, L., Duan, X., Xia, Q., Fan, X., Li, Y., Zhang, F., Peng, W., and Wang, S. (2020). High-performance porous graphene from synergetic nitrogen doping and physical activation for advanced nonradical oxidation. J. Hazard. Mater. *381*, 121010.

Xu, J., Wang, K., Zu, S., Han, B., and Wei, Z. (2010). Hierarchical nanocomposites of polyaniline nanowire arrays on graphene oxide sheets with synergistic effect for energy storage. ACS Nano *4*, 5019–5026.

Yan, Y., Li, W., and Kral, P. (2017). Enantioselective molecular transport in multilayer graphene nanopores. Nano Lett. *17*, 6742–6746.

Yusoff, M.M., Mostapa, N.R.N., Sarkar, M.S., Biswas, T.K., Rahman, M.L., Arshad, S.E., Sarjadi, M.S., and Kulkarni, A.D. (2017). Synthesis of ion imprinted polymers for selective recognition and separation of rare earth metals. J. Rare Earths *35*, 177–186.

Zheng, X., Zhang, Y., Zhang, F., Li, Z., and Yan, Y. (2018). Dual-template docking oriented ionic imprinted bilayer mesoporous films with efficient recovery of neodymium and dysprosium. J. Hazard. Mater. *353*, 496–504.

Zheng, X., Zhang, F., Liu, E., Xu, X., and Yan, Y. (2017). Efficient recovery of neodymium in acidic system by free-standing dual-template docking oriented ionic imprinted mesoporous films. ACS Appl. Mater. Interfaces *9*, 730–739.

Zhou, D., Cui, Y., Xiao, P., Jiang, M., and Han, B. (2014). A general and scalable synthesis approach to porous graphene. Nat. Commun. *5*, 4716.

iScience, Volume *24*

Supplemental Information

Nitrogen-doped nanoporous graphene induced by a multiple confinement strategy for membrane separation of rare earth

Hongxin Tan, Xin Zhang, Zhan Li, Qing Liang, Jinsheng Wu, Yanli Yuan, Shiwei Cao, Jia Chen, Juewen Liu, and Hongdeng Qiu

TABLE of CONTENTS

TRANSPARENT METHODS
Materials
Synthesis of NDNG
Characterizations
Separation of REEs

SUPPLEMENTAL FIGURES
Figure S1. Interlayer spacings of GO composites.
Figure S2. TEM images of the samples $Zn(NO_3)_2$/GO/Phe with different $Zn(NO_3)_2$ concentration.
Figure S3. XRD of NDNG.
Figure S4. Raman of NDNG.
Figure S5. N_2 adsorption−desorption isotherms of NDNG.
Figure S6. FT-IR spectra of GO, Phe/GO, Zn-hydrotalcite/Phe/GO and NDNG-3 samples.
Figure S7. TGA curves of GO, Phe/GO, Zn-hydrotalcite/Phe/GO and NDNG-3 samples under air atmosphere.
Figure S8. Typical high resolution XPS C 1s spectra of the NDNG.
Figure S9. SEM images of surface and cross-section of NDNG membranes.
Figure S10. Kinetic study of Sc^{3+} and Gd^{3+} separation through NDNG-1 membrane.
Figure S11. Separation factor of REEs as a function of the NDNG-1 membrane thickness.
Figure S12. Separation factor with different NDNG membranes of M/Sc (M = Y, La, Ce, Pr, Nd, Sm, Eu, Gd, Tb, Dy, Ho, Er, Tm, Lu.).
Figure S13. Selective separation of lanthanide M2 (Sm and Gd) and other lanthanide M1.
Figure S14. stability of NDNG membrane in acidic (pH = 3.0) solutions after 90 days.
Figure S15. Experimental equilibrium isotherm data and modeling for Sc^{3+} sorption on NDNG-3.

SUPPLEMENTAL TABLES
Table S1. Atomic Composition of NDNG and Nanoporous Graphene
Table S2. Comparison of Separation Factor with Ion Imprinted Membranes
Table S3. Langmuir Model Parameter Calculated from Adsorption Isotherm

SUPPLEMENTAL REFERENCES

TRANSPARENT METHODS

Materials

All reagents and chemicals including Natural graphite powder, amino acids and were purchased from Shanghai Aladdin Industrial Co., Ltd., Shanghai. They were reagent grade and used as received without further purification.

Synthesis of NDNG

A modified Hummers method was used for the preparation of GO from natural graphite powder(Hummers and Offeman 1958). Then the brown GO dispersion (10.0 g/L) was obtained in deionized water via ultrasonic. In a typical process, 0.3 g of phenylalanine (Phe) was dissolved into the 10 mL deionized water, then 10 mL as-prepared aqueous GO dispersion was added. Successively, the mixer of Phe and GO was stirred for approximately 30 min at room temperature. Under vigorous agitation, appropriate amount of $Zn(NO_3)_2$ (1, 2, 3, 4, 6, 8, 9 and 10 g) was added slowly, respectively. The result concentration of $Zn(NO_3)_2$ solution corresponded to 50 g/L, 100 g/L, 150 g/L, 200 g/L, 300 g/L, 400 g/L, 450 g/L and 500 g/L, respectively. Stir evenly, the mixed solution was vacuum filtered by the quantitative filter paper. After drying at 50 °C, all samples of the filter paper with GO, Phe and Zn $(NO_3)_2$ were firstly characterized by XRD with thin film analysis model, then ignited using an alcohol burner. The resulting combustion products were ultrasonicated and centrifuged with diluted HCl and deionized water several times until the eluent was neutral, then dried at 50 °C overnight under vacuum. Here, series of samples are also prepared in a similar method by changing the amount of amino acids (0.2 g, 0.1 g) with concentration of $Zn(NO_3)_2$ 500 g/L. For comparison, Alanine (Ala), no-aromatic amino acid, was used to replace Phe to prepare NDNG in a similar method. Moreover, we also changed the adding order of amino acid and $Zn(NO_3)_2$ to obtain sample of Phe/$Zn(NO_3)_2$/GO, $Zn(NO_3)_2$/Ala/GO, $Zn(NO_3)_2$/Ala/GO and Ala/$Zn(NO_3)_2$/GO, then prepared NDNG for comparing the N-doping content in the final combustion product.

$Zn(NO_3)_2$/Phe/GO: 0.3 g of phenylalanine (Phe) was dissolved into the 10 mL of deionized water, then 10 mL as-prepared aqueous GO dispersion was added. Successively, the mixer of Phe and GO was stirred for approximately 30 min at room temperature. Under vigorous agitation, 10 g of $Zn(NO_3)_2$ was added slowly. Stir evenly, the mixed solution was vacuum filtered by the quantitative filter paper. After drying at 50 °C, the sample was ignited using an alcohol burner. The resulting combustion product was ultrasonicated and centrifuged with diluted HCl and deionized water several times until the eluent was neutral, then dried at 50 °C overnight under vacuum.

Phe/$Zn(NO_3)_2$/GO: Under vigorous agitation, 10 g of $Zn(NO_3)_2$ was added into the 10 mL of deionized water, then 10 mL as-prepared aqueous GO dispersion was added. Then, 0.3 g of phenylalanine (Phe) was dissolved into the above dispersion. Stir evenly, the mixed solution was vacuum filtered directly by the quantitative filter paper. After drying at 50 °C, the sample was ignited using an alcohol burner. The resulting combustion product was ultrasonicated and centrifuged with diluted HCl and deionized water several times until the eluent was neutral, then dried at 50 °C overnight under vacuum.

$Zn(NO_3)_2$/Ala/GO: 0.16 g of alanine (Ala) was dissolved into the 10 mL of deionized water, then 10 mL as-prepared aqueous GO dispersion was added. Successively, the mixer of Ala and GO was stirred for approximately 30 min at room temperature. Under vigorous agitation, 10 g of $Zn(NO_3)_2$ was added slowly. Stir evenly, the mixed solution was vacuum filtered by the quantitative filter paper. After drying at 50 °C, the sample was ignited using an alcohol burner. The resulting combustion product was ultrasonicated and

centrifuged with diluted HCl and deionized water several times until the eluent was neutral, then dried at 50 °C overnight under vacuum.

Ala/$Zn(NO_3)_2$/GO: Under vigorous agitation, 10 g of $Zn(NO_3)_2$ was added into 10 mL of deionized water, then 10 mL as-prepared aqueous GO dispersion was added. Then, 0.16 g of alanine (Ala) was dissolved into the above dispersion. Stir evenly, the mixed solution was vacuum filtered directly by the quantitative filter paper. After drying at 50 °C, the sample was ignited using an alcohol burner. The resulting combustion product was ultrasonicated and centrifuged with diluted HCl and deionized water several times until the eluent was neutral, then dried at 50 °C overnight under vacuum.

Characterizations

All resulting NDNG samples were characterized by transmission electron microscope (TEM, FEI, USA), scanning electron microscope (SEM, HITACHI, Japan), X-ray diffraction (XRD, PANalytical, Netherlands), Raman spectroscopy (HORIBA Jobin Yvon S.A.S., France), and X-ray photoelectron spectroscopy (XPS, ThermoFisher Scientific, USA) equipped with a monochromatic Al Kα X-ray source. Nitrogen adsorption/desorption isotherms were obtained with a Micrometritics ASAP 2020M analyzer (micromeritics, USA) at 77 K, and the specific surface area was calculated from the Brunauer–Emmett–Teller (BET) plot of the N_2 adsorption isotherm. Atomic force microscopy (AFM) images were obtained on a Bruker Dimension Icon (Germany). 5 μL of diluted GO, Phe/GO, and $Zn(NO_3)_2$/Phe/GO aqueous dispersion was dropped on freshly cleaved mica and dried at room temperature to make the AFM samples, respectively.

Separation of REEs

pH Variation Study: 3 mg of NDNG-1 was first prepared by vacuum filter with polyvinylidene fluoride (PVDF) membrane to form membrane for separating of rare earth elements (REEs). The pH of a feed solution of REEs (5mM) was adjusted to 3.0. The pH tests were performed using a driven solution of different concentration of HNO_3 at various pH (1.0, 2.0 and 2.5). The pH was adjusted by diluted NH_4OH or HNO_3 solution.

Effects of membrane thickness: Because of the definite filtration area of 0.79 cm^2, the increasing amount of NDNG certainly increases the thickness of final NDNG membrane. Thus, 2 mg, 3 mg, 4 mg and 5 mg of NDNG-1 were used to prepare membranes with different thickness, respectively. The thickness of the membranes is 45 μm, 105 μm, 157 μm, and 200 μm, respectively. Subsequently, HNO_3 at pH 2 as driven solution and 5 mM of REEs as feed solution were used to perform the permeation and separation of as-obtained membranes.

3 mg of NDNG-1, NDNG-2, NDNG-3, NDNG-4, and NDNG-5, were first prepared to form membranes by vacuum filter for separating of rare earth elements. In the separation tests, the feed solutions containing rare earth ions were prepared with the desired concentration of 5 mM for each element of REEs in a nitric acid environment (pH=3.0). The driven solutions were dilute nitric acid (pH=2.0). As shown in Figure S9K, the feed and driven solutions were put into two independent polytetrafluoroethylene tanks of a made-to-order apparatus, respectively. The NDNG membrane was fixed in the middle of the two tanks with exposed membrane diameter of 1 cm. In order to avoid possible concentration polarization effect near the membrane, magnetic stirring was used both in the feed and permeate solution. In general tests, 5 mL of driven solution after separated for 0.5 h was used to detect elemental quantification of the various elements by inductively coupled plasma mass spectrometry (ICP-MS). The experiments were repeated three times to get standard deviations.

Permeation rate (P) is $\frac{C_t V}{S \times t}$, C_t is the concentration of REEs at a certain time in driven solution, unit is *mol/L*; V is the volume of the driven solution, unit is L; S is the effective filter area of NDNG membrane, unit is m^2; t is time, unit is h. separation factor $\alpha = \frac{P_1}{P_2}$, p_1 is the permeation rate of the one ion, p_2 is the permeation rate of the other ion.

Computational Methodology

The density functional theory (DFT) calculations were used to calculate the electronic energies. Unconstrained geometry optimizations were performed by the functional B3LYP (Becke, 1993; Lee et al., 1988), with Grimmes DFT-D3 dispersion correction using the Becke-Johnson damping function (Grimme et al., 2011), and the def_2-SVP (Weigend and Ahlrichs, 2005) basis set was adopted. All energies were corrected for the basis set superposition error (BSSE) using the method of Boys and Bernardi (Boys and Bernardi, 1970). All quantum chemistry calculations were performed with Gaussian 16, revision B01 (Thompson and Frechet, 2008). The electrostatic potential (ESP) calculations and (Electron Localization Function) ELF analysis were carried out by using the Multiwfn software package (Revision 3.3.8)(Lu and Chen, 2012), and the isosurface maps were rendered by the VMD 1.9.2 program (Humphrey et al., 1996) based on the outputs of Multiwfn.

Isotherm Adsorption Studies

The pH of all solutions was adjusted to 3, and the REEs concentrations ranging from 0.0031 to 0.125 mM were used to determine the maximum adsorption capacity. Above solutions were kept in a shaker operating at 230 rpm for 24 h to reach the adsorption equilibrium. The concentrations of the remaining REEs were measured by ICP-MS. Adsorption capacity Q_e (mg/g) of NDNG-3 was calculated by the following equation

$$Q_e = (C_i - C_e) \times \frac{V}{M}$$

where C_i (mg/L) and C_e (mg/L) represent initial and equilibrium concentrations of the REEs in solution, respectively. V (L) and M (g) are the volume of the testing solution and the amount of the sorbents NDNG-3, respectively.

SUPPLEMENTAL FIGURES

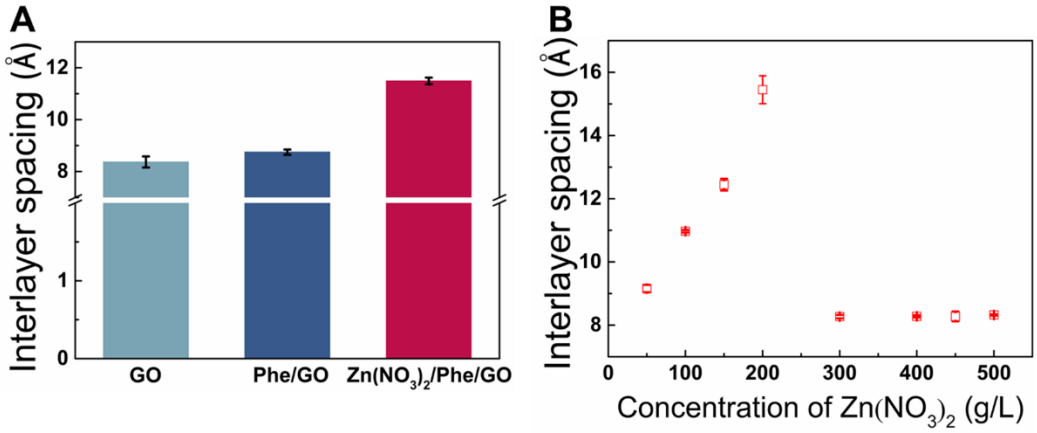

Figure S1. Interlayer spacings of GO composites, related to Figure 1.

(A) Interlayer spacing of GO and GO composites. (B) Interlayer spacing of $Zn(NO_3)_2$/Phe/GO with $Zn(NO_3)_2$ concentration.

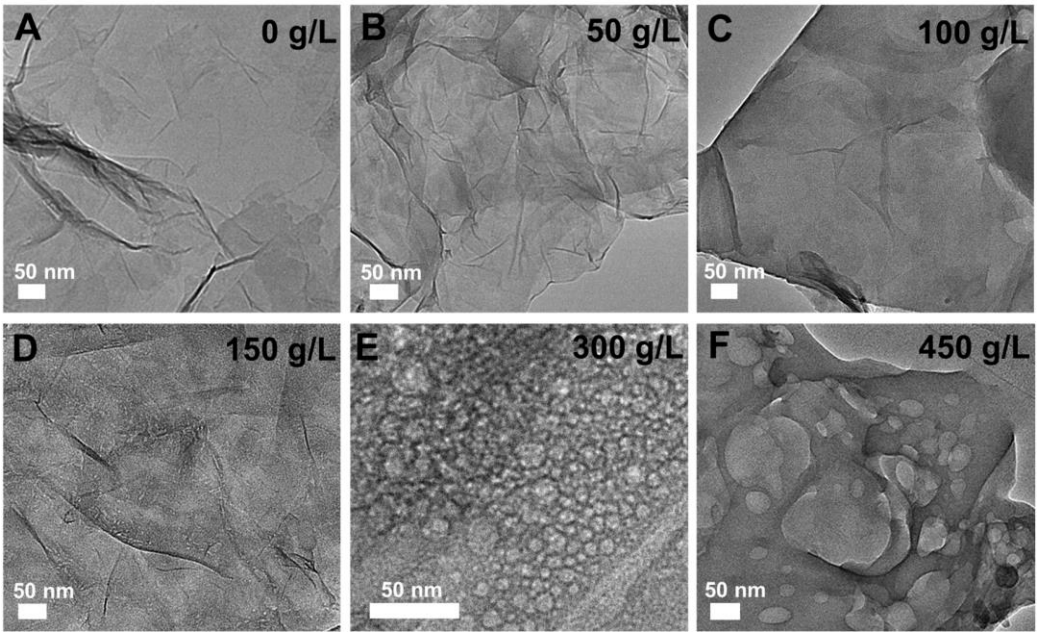

Figure S2. TEM images of the samples $Zn(NO_3)_2$/GO/Phe with different $Zn(NO_3)_2$ concentration, related to Figure 1.

(A) 0 g/L (GO). (B) 50 g/L. (C) 100 g/L. (D) 150 g/L. (E) 300 g/L. (F) 450 g/L.

With the increase of $Zn(NO_3)_2$•$6H_2O$ concentrations, the amount of nitrate crystal water retained between the GO layers gradually increases. When heating and drying after filtration, the larger amount of crystal water from $Zn(NO_3)_2$ can produce the larger volume of vapor bubbles. As these vapor bubbles burst, the larger volume of bubbles would cause the larger size of pores on the surface of hydrotalcite. Therefore, a larger pore of hydrotalcite was observed at higher concentrations of $Zn(NO_3)_2$.

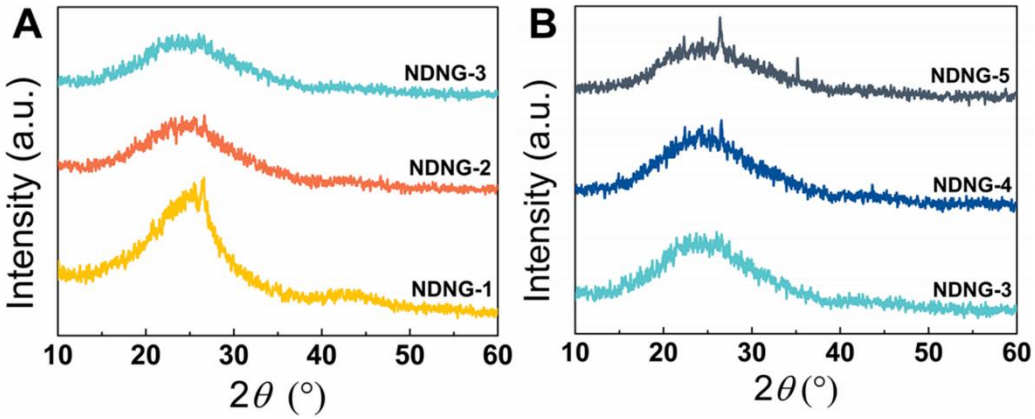

Figure S3. XRD of NDNG, related to Figure 2.

(A) NDNG-1, NDNG-2 and NDNG-3. (B) NDNG-3, NDNG-4 and NDNG-5.

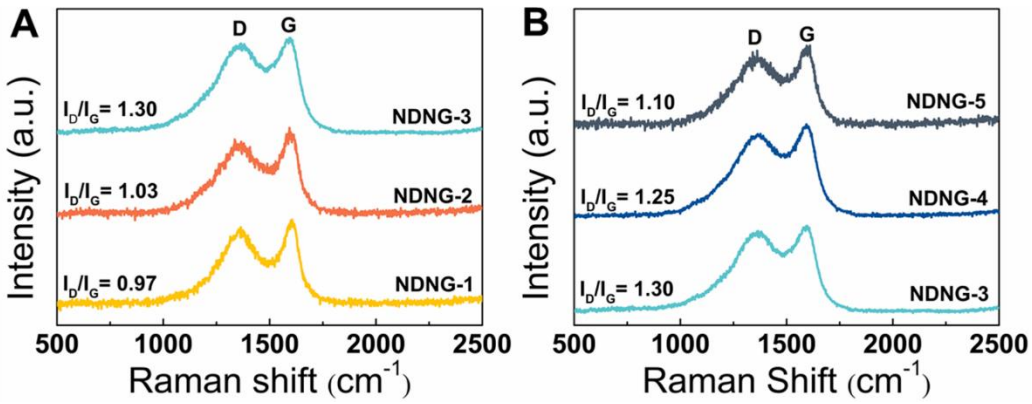

Figure S4. Raman of NDNG, related to Figure 2.

(A) NDNG-1, NDNG-2 and NDNG-3. (B) NDNG-3, NDNG-4 and NDNG-5.

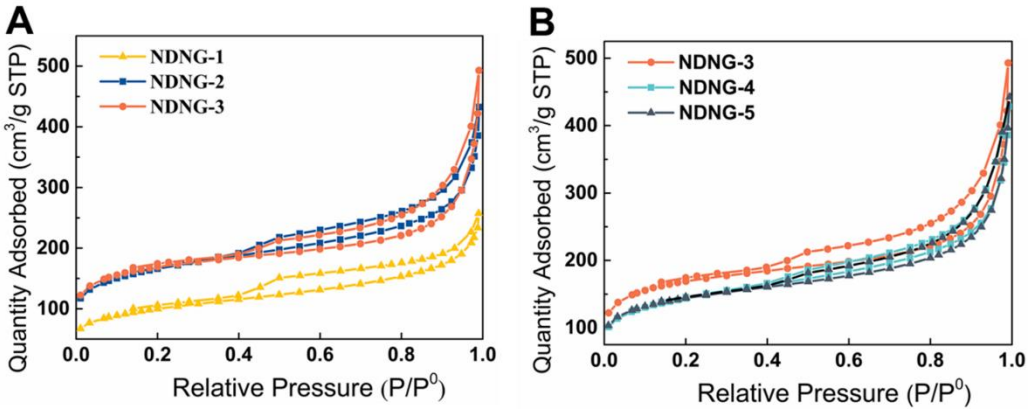

Figure S5. N_2 adsorption−desorption isotherms of NDNG, related to Figure 2.

(A) NDNG-1, NDNG-2 and NDNG-3. (B) NDNG-3, NDNG-4 and NDNG-5.

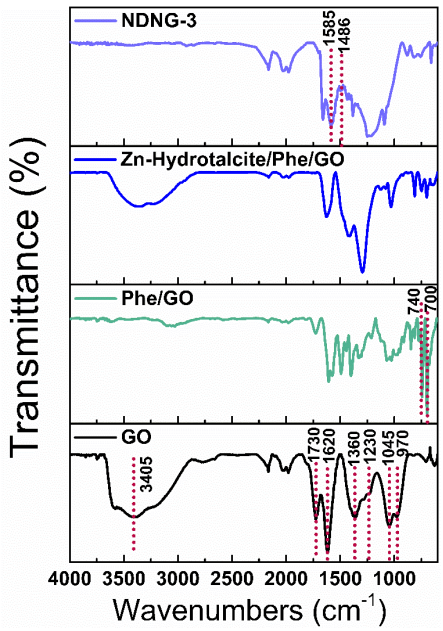

Figure S6. FT-IR spectra of GO, Phe/GO, Zn-hydrotalcite/Phe/GO and NDNG-3 samples, related to Figure 2.

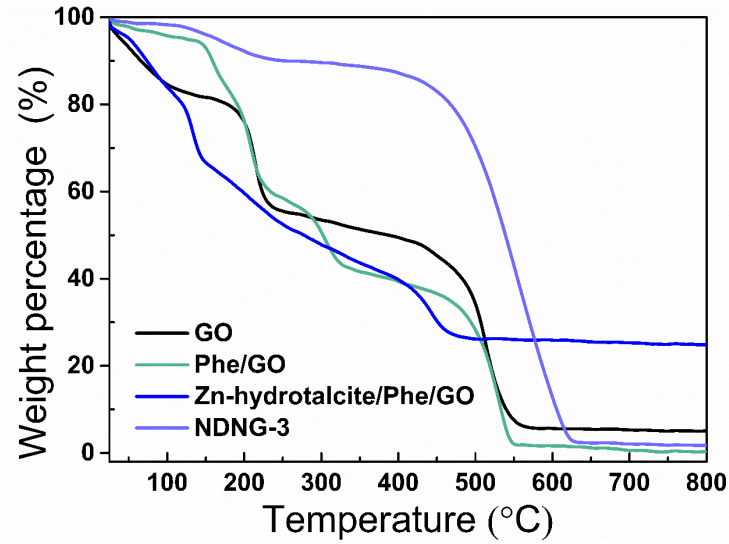

Figure S7. TGA curves of GO, Phe/GO, Zn-hydrotalcite/Phe/GO and NDNG-3 samples under air atmosphere, related to Figure 2.

The chemical structures of the GO, Phe/GO, Zn-hydrotalcite/Phe/GO, and NDNG-3 samples were characterized to monitor the synthetic processes by Fourier transform infrared (FT-IR) (Figure S6). As shown in Figure S6, there are many O-containing groups that exist on GO sheets. The characteristic functional groups of GO were observed at 3405 cm^{-1} (C-OH), 1730 cm^{-1} (C=O), 1620 cm^{-1} (C=C), 1360 cm^{-1} (C–OH), 1230 cm^{-1}, 1045 cm^{-1} and 970 (C–O) cm^{-1}, respectively. Compared with that of pure GO, the FT-IR spectrum of Phe/GO showed several differences from that of GO, such as the peaks at 740 and 700 cm^{-1} associating with Phe. The result suggests that after mixing with GO, Phe was successfully adsorbed by GO. After the formation of the Zn-hydrotalcite on the Phe/GO sheets, some prominent peaks shifted largely or disappeared, which was due to strongly interactions between Zn-hydrotalcite and functional groups on the Phe/GO sheets. It should be noted that the peak at 1730 cm^{-1} of GO disappeared and new absorption peaks at 1486 cm^{-1} and 1585 cm^{-1} corresponding to C-N and C=N stretching appeared, indicating that most of the O-containing groups were removed and NDNG was successfully prepared.

In order to understand the observations, thermogravimetric analysis (TGA) tests were carried out on several samples (Figure S7). TGA of the GO has a mass loss before 100 °C due to the removal of trapped water between the sheets of GO. The mass removal in the range 200–230 °C was attributed to the decomposition of less stable oxygen functionalities. Between 230 and 800 °C, a gradual weight loss was observed and can be related to the removal of more stable oxygen functionalities and graphitic regions. It is worth noting that the presence of Phe and Zn-hydrotalcite in the samples of Phe/GO and Zn-hydrotalcite/Phe/GO remarkably changes the thermal process of GO, suggesting that the structure of Zn-hydrotalcite/Phe/GO was successfully prepared.

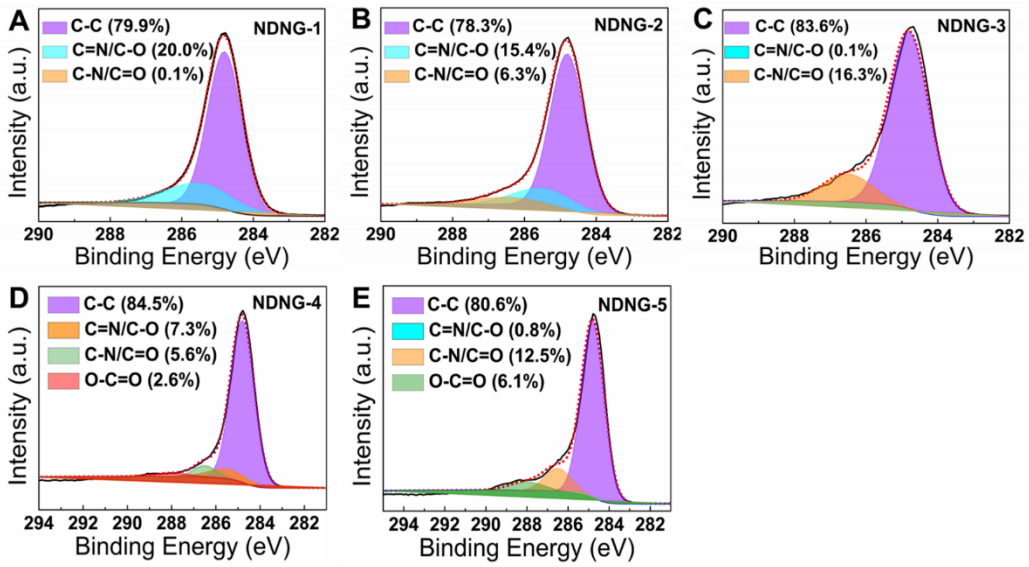

Figure S8. Typical high resolution XPS C 1s spectra of the NDNG, related to Figure 3.

(A) NDNG-1. (B) NDNG-2. (C) NDNG-3. (D) NDNG-4. (E) NDNG-5.

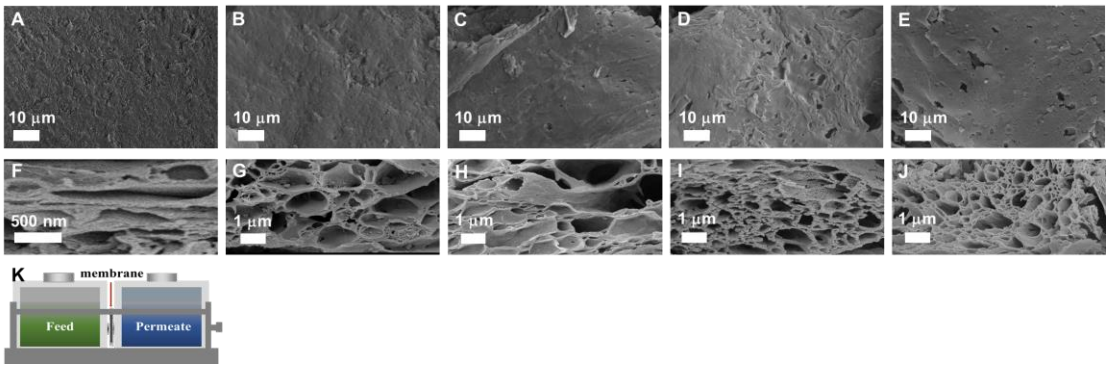

Figure S9. SEM images of surface and cross-section of NDNG membranes, related to Figure 4.

(A-E) SEM image of the surface morphology of NDNG membranes prepared with NDNG-1 (A), NDNG-2 (B), NDNG-3 (C), NDNG-4 (D), and NDNG-5 (E). (F-J) SEM image of the cross-sectional view of NDNG membranes prepared with NDNG-1 (F), NDNG-2 (G), NDNG-3 (H), NDNG-4 (I), and NDNG-5 (J). (K) schematic of ion separation equipment, REEs solution and HNO_3 solution are placed as the feed and permeate solutions, respectively.

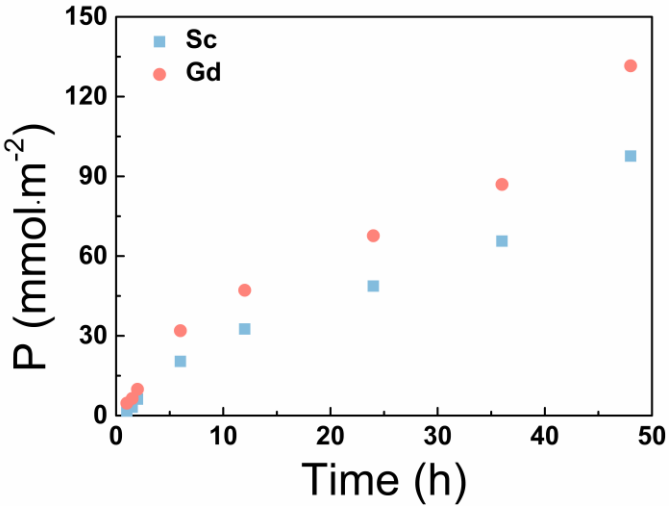

Figure S10. Kinetic study of Sc^{3+} and Gd^{3+} separation through NDNG-1 membrane, related to Figure 4.

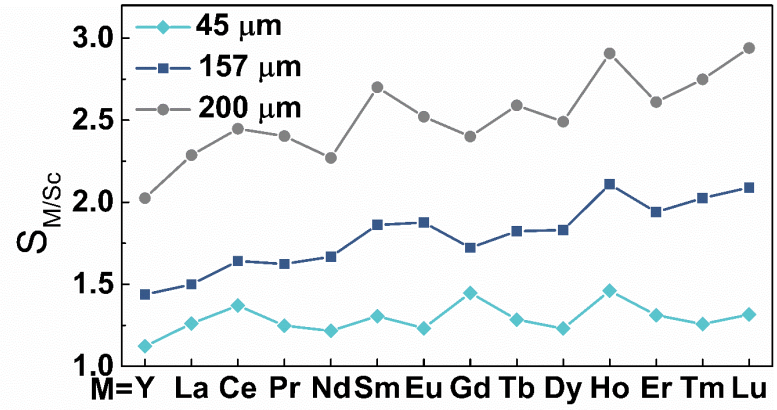

Figure S11. Separation factor of REEs as a function of the NDNG-1 membrane thickness, related to Figure 4.

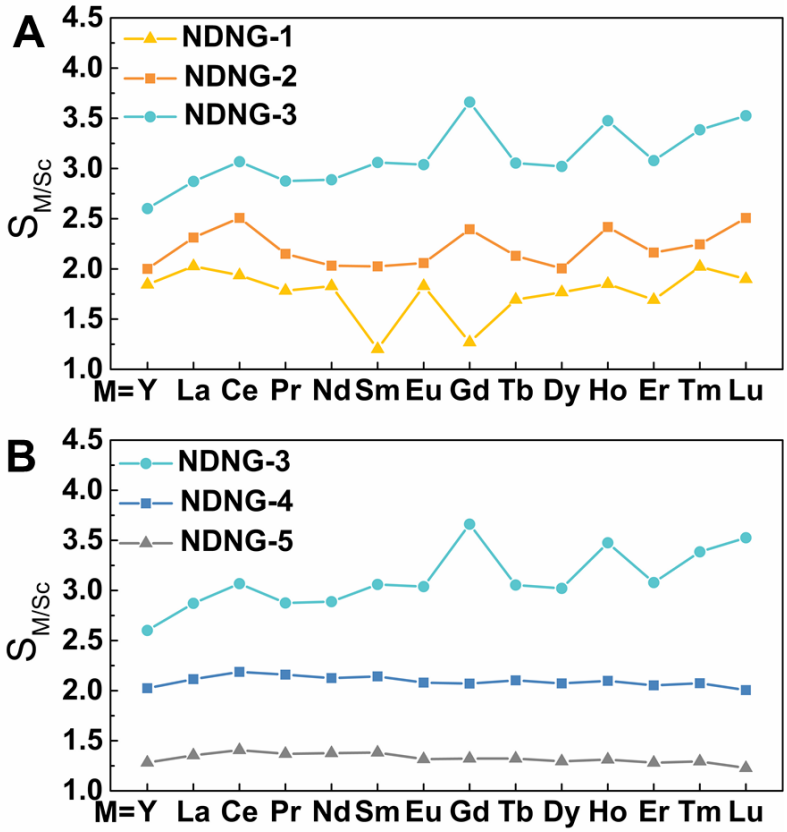

Figure S12. Separation factor with different NDNG membranes of M/Sc (M = Y, La, Ce, Pr, Nd, Sm, Eu, Gd, Tb, Dy, Ho, Er, Tm, Lu.), related to Figure 4.

(A) NDNG-1, NDNG-2, NDNG-3. (B) NDNG-3, NDNG-4, and NDNG-5. The feed solution has a concentration of 5 mM for all elements at a pH of 3.0; The driven solution is dilute nitric acid at a pH of 2.0.

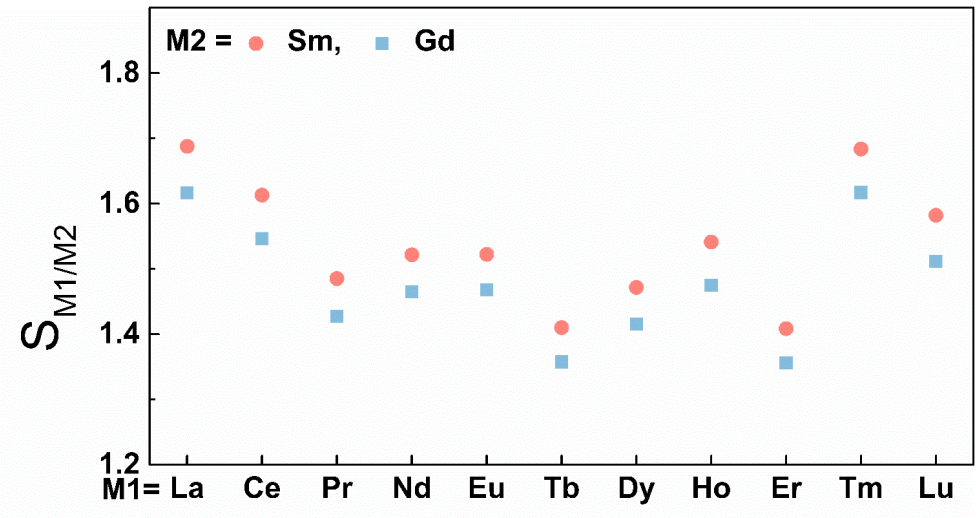

Figure S13. Selective separation of lanthanide M_2 (Sm and Gd) and other lanthanide M_1 for NDNG-3 membrane, related to Figure 4.

M_1 is selected from the lanthanide elements except Sm and Gd, and M_2 is chosen from Sm and Gd.

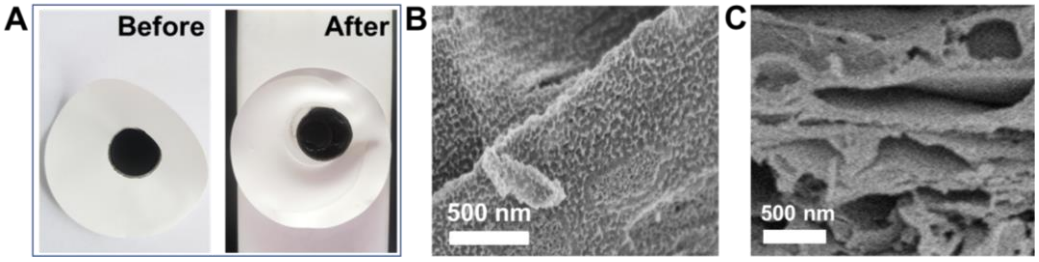

Figure S14. stability of NDNG membrane in acidic (pH = 3.0) solutions after 90 days, related to Figure 4.

(A) Photos of a NDNG membrane before and after separation of REEs. SEM images of surface (B) and cross-section (C) of NDNG membrane prepared with NDNG-1 after separation of REEs.

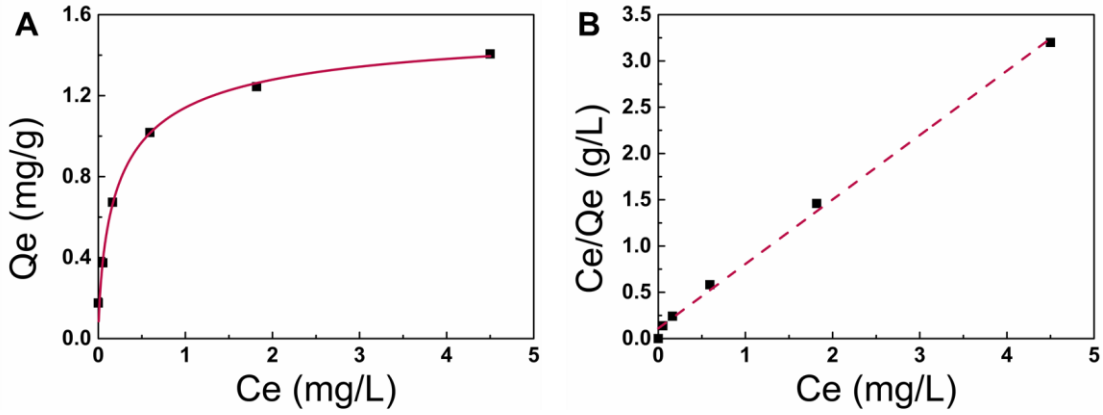

Figure S15. Experimental equilibrium isotherm data and modeling for Sc^{3+} sorption on NDNG-3, related to Figure 5.

(A) Equilibrium isotherms for the adsorption of Sc^{3+} in the presence of other REEs by NDNG-3, pH = 3, m = 4 mg, V= 5 mL. (B) Fitting for the Langmuir model.

SUPPLEMENTAL TABLES

Table S1. Atomic Composition of NDNG and Nanoporous Graphene, related to Figure 3

Sample	C %	N %	O %
$Zn(NO_3)_2$/Phe/GO	78.6	2.5	17.0
Phe/$Zn(NO_3)_2$/ GO	85.4	1.9	11.1
$Zn(NO_3)_2$/Ala/GO	80.0	0.9	16.6
Ala/$Zn(NO_3)_2$/ GO	82.1	0.8	15.0
$Zn(NO_3)_2$/ GO	83.2	0.0	14.2

All samples were performed in triplicates, and only the average is presented.

As shown in Table S1, the nitrogen element cannot be detected in the product of the sample $Zn(NO_3)_2$/GO (nanoporous graphene).

Table S2. Comparison of Separation Factor with Ion Imprinted Membranes, related to Figure 4

No.	Target ion	Interfering ion	Separation Factor	Ref.
1	Eu^{3+}	La^{3+}, Gd^{3+}, Sm^{3+}	3.82, 3.47, 3.34	[Chen et al., 2018)]
2	Gd^{3+}	La^{3+}, Ce^{3+}	3.50, 2.23	[Li et al., 2015]
3	Ce^{3+}	Fe^{3+}	3.2	[Liu et al., 2014]
4	Gd^{3+}	La^{3+}, Eu^{3+}	2.91, 2.49	[Cui et al., 2019]
5	Nd^{3+}, Dy^{3+}	Pr^{3+}, Tb^{3+}	3.02, 4.16	[Zheng et al., 2018]
6	Nd^{3+}	Pr^{3+}	3.56	[Zheng et al., 2017]
7	Dy^{3+}	Nd^{3+}	3.33	[Liu et al., 2017]
8	Sc^{3+}	Other REEs	3.7	This work

Table S3. Langmuir Model Parameter Calculated from Adsorption Isotherm, related to Figure 5

Sample	K_L (L/mg)	Q_m (mg/g)	R^2
NDNG-3	6.2823	1.4369	0.9958

SUPPLEMENTAL REFERENCES

Becke, A.D. (1993). DENSITY-FUNCTIONAL THERMOCHEMISTRY .3. THE ROLE OF EXACT EXCHANGE. J. Chem. Phys. *98*, 5648-5652.

Boys, S.F., and Bernardi, F. (1970). CALCULATION OF SMALL MOLECULAR INTERACTIONS BY DIFFERENCES OF SEPARATE TOTAL ENERGIES-SOME PROCEDURES WITH REDUCED ERRORS. Mol. Phys. *19*, 553-566.

Grimme, S., Ehrlich, S., and Goerigk, L. (2011). Effect of the Damping Function in Dispersion Corrected Density Functional Theory. J. Comput. Chem. *32*, 1456-1465.

Hummers, W.S., Offeman, R.E., 1958. PREPARATION OF GRAPHITIC OXIDE. J. Am. Chem. Soc. *80*, 1339-1339.

Humphrey, W., Dalke, A., and Schulten, K. (1996). VMD: Visual molecular dynamics. J. Mol. Graphics Modell. *14*, 33-38.

Lee, C.T., Yang, W.T., and Parr, R.G. (1988). DEVELOPMENT OF THE COLLE-SALVETTI CORRELATION-ENERGY FORMULA INTO A FUNCTIONAL OF THE ELECTRON-DENSITY. Physical Review B *37*, 785-789.

Lu, T., and Chen, F. (2012). Multiwfn: A multifunctional wavefunction analyzer. J. Comput. Chem. *33*, 580-592.

Thompson, B.C., and Frechet, J.M.J. (2008). Organic photovoltaics-Polymer-fullerene composite solar cells. Angew. Chem., Int. Ed. *47*, 58-77.

Weigend, F., and Ahlrichs, R. (2005). Balanced basis sets of split valence, triple zeta valence and quadruple zeta valence quality for H to Rn: Design and assessment of accuracy. Phys. Chem. Chem. Phys. *7*, 3297-3305.